Theses and Dissertations   1. Thesis and Dissertation Collection, all items

12

INFERRING ICE BASAL ROUGHNESS FROM HIGH RESOLUTION SYNTHETIC APERTURE RADAR SATELLITE IMAGERY

Green, Terrance O., Sr.

Monterey, CA; Naval Postgraduate School

https://hdl.handle.net/10945/64174

NAVAL POSTGRADUATE SCHOOL

MONTEREY, CALIFORNIA

THESIS

**INFERRING ICE BASAL ROUGHNESS FROM
HIGH RESOLUTION SYNTHETIC APERTURE RADAR
SATELLITE IMAGERY**

by

Terrance O. Green Sr.

December 2019

Thesis Advisor:	Timothy P. Stanton
Second Reader:	William J. Shaw

Approved for public release. Distribution is unlimited.

THIS PAGE INTENTIONALLY LEFT BLANK

REPORT DOCUMENTATION PAGE		*Form Approved OMB No. 0704-0188*

Public reporting burden for this collection of information is estimated to average 1 hour per response, including the time for reviewing instruction, searching existing data sources, gathering and maintaining the data needed, and completing and reviewing the collection of information. Send comments regarding this burden estimate or any other aspect of this collection of information, including suggestions for reducing this burden, to Washington headquarters Services, Directorate for Information Operations and Reports, 1215 Jefferson Davis Highway, Suite 1204, Arlington, VA 22202-4302, and to the Office of Management and Budget, Paperwork Reduction Project (0704-0188) Washington, DC 20503.

1. AGENCY USE ONLY *(Leave blank)*	2. REPORT DATE December 2019	3. REPORT TYPE AND DATES COVERED Master's thesis	
4. TITLE AND SUBTITLE INFERRING ICE BASAL ROUGHNESS FROM HIGH RESOLUTION SYNTHETIC APERTURE RADAR SATELLITE IMAGERY		**5. FUNDING NUMBERS**	
6. AUTHOR(S) Terrance O. Green Sr.			
7. PERFORMING ORGANIZATION NAME(S) AND ADDRESS(ES) Naval Postgraduate School Monterey, CA 93943-5000		**8. PERFORMING ORGANIZATION REPORT NUMBER**	
9. SPONSORING / MONITORING AGENCY NAME(S) AND ADDRESS(ES) N/A		**10. SPONSORING / MONITORING AGENCY REPORT NUMBER**	

11. SUPPLEMENTARY NOTES The views expressed in this thesis are those of the author and do not reflect the official policy or position of the Department of Defense or the U.S. Government.

12a. DISTRIBUTION / AVAILABILITY STATEMENT Approved for public release. Distribution is unlimited.	12b. DISTRIBUTION CODE A

13. ABSTRACT (maximum 200 words)

During the past decade, direct measurements of ocean turbulent friction velocity and current velocity profiles have been conducted in polar regions using Autonomous Ocean Flux Buoys (AOFBs). Recent use of Synthetic Aperture Radar (SAR) imagery augmented by digital image processing techniques has proven to be an effective means of monitoring ice conditions. This study examines the relationship between ice-ocean drag coefficients and SAR-derived open water area, feature perimeter and ice ridge length. Drag coefficients are calculated from AOFB current speed and friction velocity measurements collected between 5 October and 29 October 2018 in the Beaufort Sea. Threshold and image processing techniques were applied to a total of 82 SAR images at 6 logarithmically spaced radial upstream distances from the AOFB to classify the three ice feature types. The results indicate that sparse statistics associated with the size and image processing limitations within the near field of the AOFB, coupled with a lack of high resolution satellite imagery, stifled the SAR's ability to accurately characterize the relationship between ice-ocean drag coefficients and ice feature density distributions within upstream radial sectors within the buoy-centered 20 x 20 km SAR images.

14. SUBJECT TERMS Arctic Ocean, Canada Basin, Beaufort Sea, transpolar drift sea ice, ice concentration, mixed layer, ice ocean boundary layer, inertial motion, inertial oscillations, shear velocity, friction velocity, drag coefficient, surface roughness length, turbulence, oceanic forcing, wind forcing, ice speed, ice drift, Autonomous Ocean Flux Buoy, Ice-Tethered Profiler, Synthetic Aperture Radar, RADARSAT-2, image processing, sea ice leads, sea ice ridges, threshold, Derivative Edge Detection			15. NUMBER OF PAGES 79
			16. PRICE CODE

17. SECURITY CLASSIFICATION OF REPORT Unclassified	18. SECURITY CLASSIFICATION OF THIS PAGE Unclassified	19. SECURITY CLASSIFICATION OF ABSTRACT Unclassified	20. LIMITATION OF ABSTRACT UU

NSN 7540-01-280-5500

Standard Form 298 (Rev. 2-89)
Prescribed by ANSI Std. 239-18

THIS PAGE INTENTIONALLY LEFT BLANK

Approved for public release. Distribution is unlimited.

**INFERRING ICE BASAL ROUGHNESS FROM HIGH RESOLUTION
SYNTHETIC APERTURE RADAR SATELLITE IMAGERY**

Terrance O. Green Sr.
Lieutenant, United States Navy
BS, University of Southern Mississippi, 2009

Submitted in partial fulfillment of the
requirements for the degree of

**MASTER OF SCIENCE IN METEOROLOGY AND
PHYSICAL OCEANOGRAPHY**

from the

**NAVAL POSTGRADUATE SCHOOL
December 2019**

Approved by: Timothy P. Stanton
                Advisor

                William J. Shaw
                Second Reader

                Peter C. Chu
                Chair, Department of Oceanography

THIS PAGE INTENTIONALLY LEFT BLANK

ABSTRACT

During the past decade, direct measurements of ocean turbulent friction velocity and current velocity profiles have been conducted in polar regions using Autonomous Ocean Flux Buoys (AOFBs). Recent use of Synthetic Aperture Radar (SAR) imagery augmented by digital image processing techniques has proven to be an effective means of monitoring ice conditions. This study examines the relationship between ice-ocean drag coefficients and SAR-derived open water area, feature perimeter and ice ridge length. Drag coefficients are calculated from AOFB current speed and friction velocity measurements collected between 5 October and 29 October 2018 in the Beaufort Sea. Threshold and image processing techniques were applied to a total of 82 SAR images at 6 logarithmically spaced radial upstream distances from the AOFB to classify the three ice feature types. The results indicate that sparse statistics associated with the size and image processing limitations within the near field of the AOFB, coupled with a lack of high resolution satellite imagery, stifled the SAR's ability to accurately characterize the relationship between ice-ocean drag coefficients and ice feature density distributions within upstream radial sectors within the buoy-centered 20 x 20 km SAR images.

THIS PAGE INTENTIONALLY LEFT BLANK

TABLE OF CONTENTS

LIST OF FIGURES

LIST OF ACRONYMS AND ABBREVIATIONS

2-D	two- dimensional
3-D	three-dimensional
AA	Arctic amplification
ADCP	Acoustic Doppler Current Profiler
AIDJEX	Arctic Ice Dynamics Joint Exercise
CESM	Community Earth System Model
DoD	Department of Defense
ERS	European Remote Sensing
ESA	European Space Agency
EW	Extra-wide Swath Mode
GCM	Global Climate Model
GPS	Global Positioning System
IMB	ice mass balance
IOBL	ice-ocean boundary layer
ITP	Ice-Tethered Profiler
MATLAB	matrix laboratory
MIZ	marginal ice zone
MIZ DRI	Marginal Ice Zone Department of Research Initiative
MR	medium resolution
NPS	Naval Postgraduate School
ONR	Office of Naval Research
Radar	radio detection and ranging
SAR	Synthetic Aperture Radar
SHEBA	Surface Heat Budget of the Arctic
SLAR	Side-Looking Airborne Radar
SODA DRI	Stratified Ocean Dynamics of the Arctic Department of Research Initiative
USN	United States Navy
WHOI	Woods Hole Oceanography Institute
WSC	West Svalbard Current

THIS PAGE INTENTIONALLY LEFT BLANK

ACKNOWLEDGMENTS

THIS PAGE INTENTIONALLY LEFT BLANK

I. INTRODUCTION

A. MOTIVATION

In the last fifteen years, summer Arctic sea ice extent has been diminishing at rates that exacerbates known responses, like cloud radiative forcing and ice-ocean albedo feedbacks, while initiating new and unforeseen effects, such as albedo-related terrestrial warming. The impact of these changes is already being realized through the way the atmosphere-ice-ocean interface distributes energy into the atmosphere and upper ocean through variations in sea ice. As a result, ice-frozen areas in the Arctic may become permanently open water. These changes present opportunities for expanded navigation, resource accessibility and extraction, such as oil and natural gas, as well as the primary cause for escalations between bordering countries. This is a real problem with worldwide focus and implications that are of particular interest to the U.S. Navy (USN), being contrary to the USN's strategic outlook for the Arctic, which is to ensure the Arctic remains a stable, conflict-free region (Chief of Naval Operation's Strategic Outlook for the Arctic 2019).

B. STUDY OBJECTIVES

Previous remote-sensed data and imaging technologies have used visible imagery for ice motion observation and ice state estimation. For example, downward-looking video cameras have been used on aircraft to access new ice formation and open water determination (Tschudi et al. 1997). Moreover, shipboard vessels with organic camera systems have been used to accurately estimate and compare sea ice concentration with satellite passive microwave radiometers. Although camera imagery, particularly visible, can be used to provide sea ice information on a sub-grid scale (Zhang and Skjetne 2018), the inability to capture sea ice data in cloudy weather and reduced visibility is a major problem. Furthermore, in the last decade the temporal and spatial coverage of Synthetic Aperture Radar (SAR) imagery has provided a potential source of long time-series mapping of ice conditions across the Arctic, including areas surrounding unmanned remote sensing platforms (e.g., Autonomous Ocean Flux Buoys [AOFBs]). This study seeks to investigate the relationship between AOFB-derived local ocean friction velocities and ice-

1

ocean drag coefficients to SAR-derived ice surface characteristics, and ice types at radial distances from AOFBs. This study seeks to answer the questions: does the application of image processing techniques enhance an understanding of the relationship between ice-ocean drag coefficients and ice feature distribution and concentration? Can satellite and observational techniques be used to infer ice dynamic roughness? SAR imagery time series coincident with AOFB observations will be sectored by ice floe drift and analyzed to compare upstream ice roughness features with observed ocean friction velocities and calculated drag coefficients. We hypothesize that local roughness characteristics directly affecting the AOFB stress measurements are typical of 10 km scale model grid cells, enabling a SAR analysis technique applicable to regional scale models that provides high resolution representation of ice-roughness induced turbulence at sub-grid scale levels.

C.   BACKGROUND

Due to a collection of processes underlying Arctic amplification (AA), the empirical record of disproportionately higher temperatures in the Arctic region than other regions on the planet, the sea-ice cover of the Arctic ocean is on the verge of totally disappearing in summer. The atmosphere-ice-ocean interface (Arctic system) is experiencing a steady reduction in late summer sea ice extent and multi-year ice (MYI) at rates not seen in recent history. The National Snow and Ice Center (NSIDC) defines sea ice extent as "a measurement of the area of ocean where there is at least some sea ice," and MYI as "ice that has survived at least one melt season." The change to the Arctic sea ice cover has been captured by satellite observations dating back to 1979 (Figure 1). Minimum summer (September) of -7.8% and maximum winter (March) of -1.8% ice extent estimates before the modern satellite period (1953–1979) have declined at a steady rate. This negative trend increased to -9.1% for September and -2.9% for March during the period from 1979–2006 (Stroeve et al. 2007) and implies a continuing downward trend could prevent winter sea ice regeneration. Regional Arctic models that account for atmospheric and oceanic coupling agree that within the next 10–50 years, the Arctic will be nearly ice free in the summer. Observations measured on the Arctic coast, near Point Barrow, Alaska, suggest a direct correlation between the distribution of oceanic speed in the upper ocean and ice concentration changes. During the cold season, the strong Alaska Coastal Current

has been documented to carry ~67% of the oceanic heat from the Chukchi Sea into the Beaufort Sea. This is noteworthy because it affects upper ocean mixing and generates eddies that migrate across the Beaufort basin and provide warm water entrainment that can contribute to ice melting (Maslowski et al. 2014).
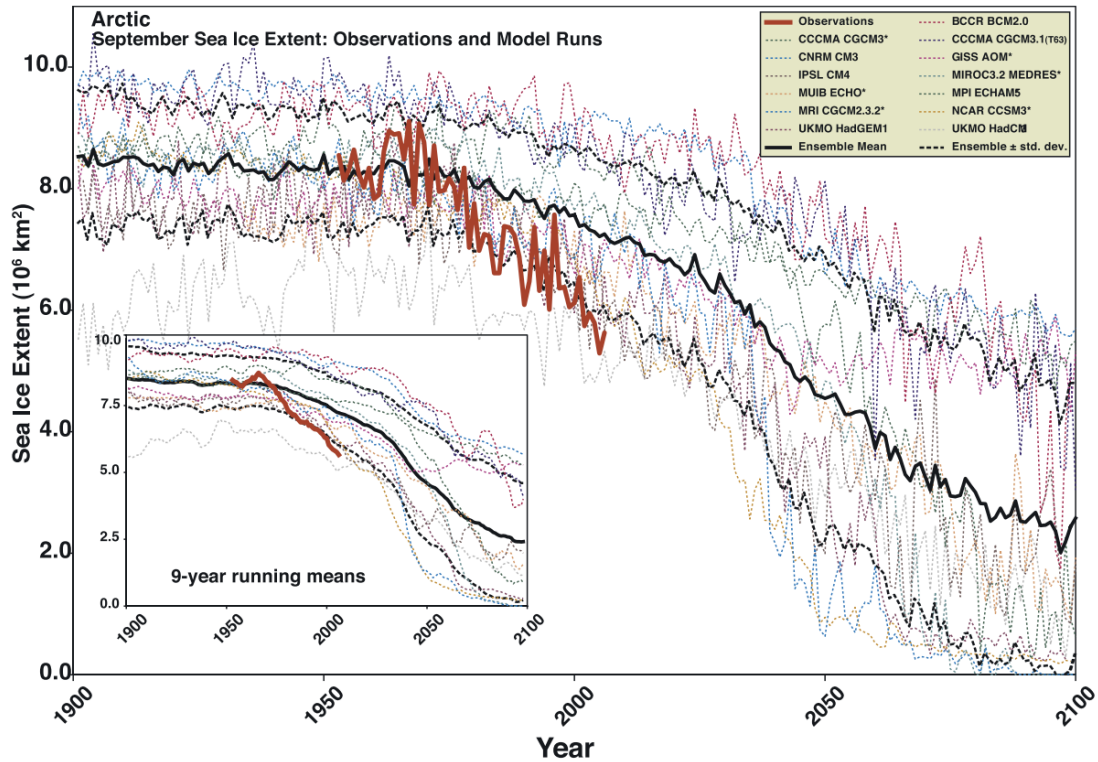
Observations are colored red. The multi-model ensemble mean is represented by the solid black line and standard deviation represented by the black dotted line.

Figure 1.   September sea ice extent model comparison.
Source: Stroeve (2007).

In addition to AOFBs, co-located Ice-Tethered Profiler (ITP) and Ice Mass Balance (IMB) buoys have been deployed as instrument clusters on ice floes since 2005. These instruments have observed an area of abnormally warm water from the surface to ~60m depth, implying the dynamic transport of heat into the mixed layer from mesoscale eddy influence (Figure 2). Therefore, mesoscale eddy induced entrainment of warmer temperature during the winter can effectively slow down sea ice growth (Haynes 2010).

Subsequently, thinner sea ice cover leading into the melt season (June/July) compounds the previous effects and allows melting of existing sea ice much earlier than the preceding year.
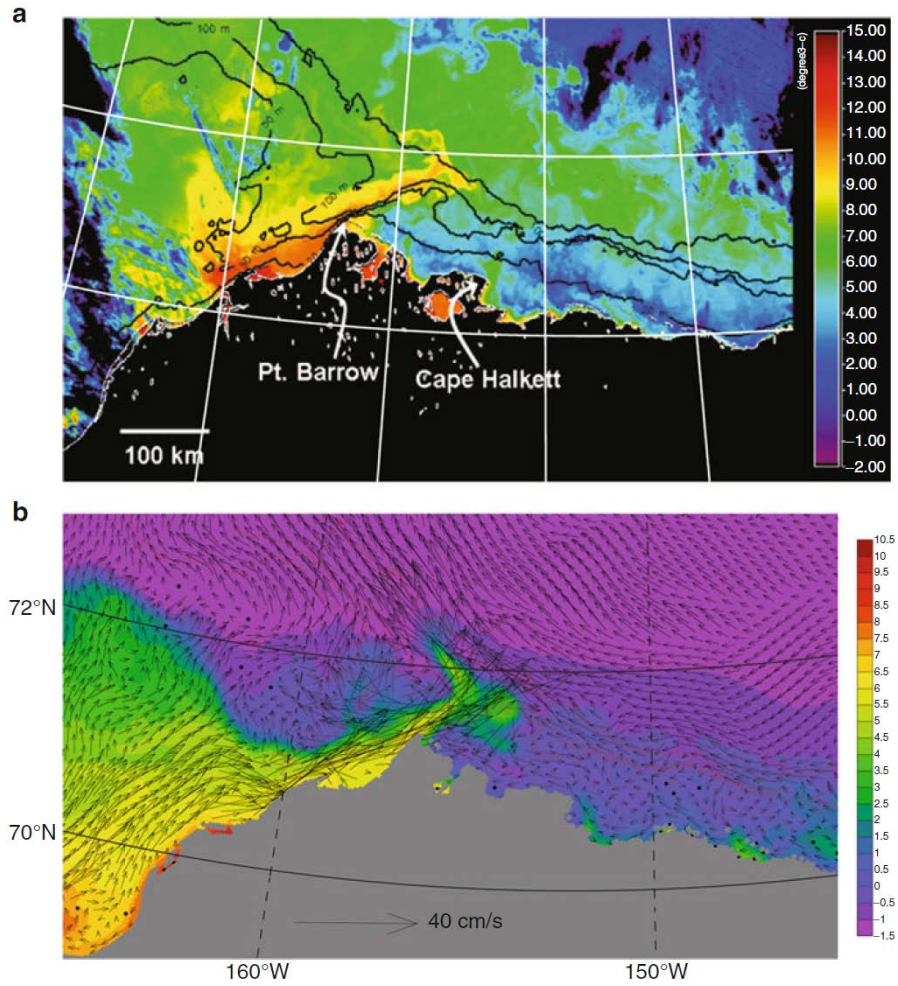
(a) Sea surface temperatures (°C) from the Moderate Resolution Imaging Spectroradiometer (b) temperature (color shading; °C) and velocity (vectors; cm s ^-1) at a surface layer of 0–5 m from the Naval Postgraduate School (NPS) Arctic Modeling Effort model.

Figure 2.   Observed surface temperatures within the Alaskan Coastal Current. Source: Malowski (2014).

The loss of MYI and increased open water fraction will have profound geopolitical effects. Declining summer sea ice extent and increasing open water fractions have relaxed

the stigma of the Arctic being unsuitable for exploration. National security concerns will escalate, as undiscovered reserves of oil, natural gas and large deposits of rare earth metals become a globally viable commodity, particularly for countries along the Arctic border (National Security Strategy, 2017). Russia is strengthening its position to corner the growing commercial markets in the Arctic through an impressive production of the largest and most powerful nuclear icebreakers ever built (RFE/RL 2019). Furthermore, as transpolar routes continue to open up (Figure 3), the potential for ship-to-sea ice and or iceberg interaction will increase (Commander Kristen Serumgard, *Commander, International Ice Patrol* 2019).
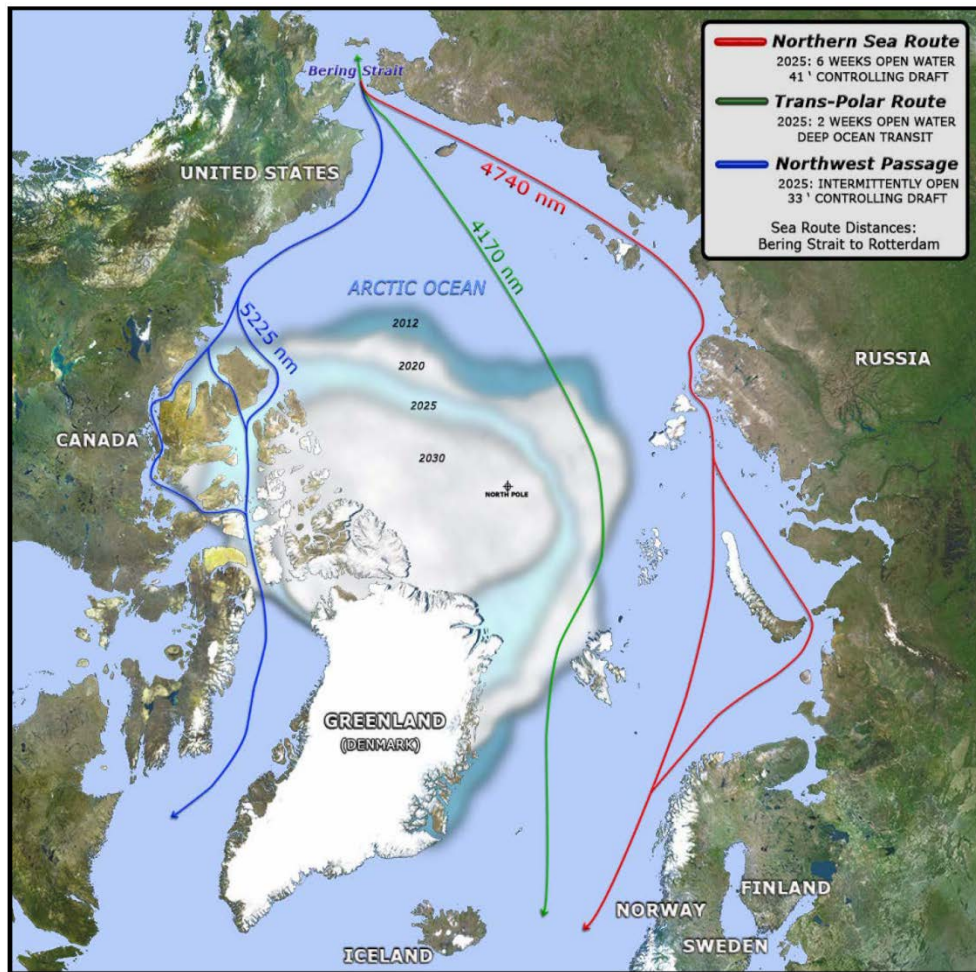
Figure 3.   U.S. Navy consensus assessment of sea ice extent
minima. Source: United States Navy graphic (2014).

The presence of MYI around the Canadian archipelago, which has clogged the channels of the Northwest Passage, is rapidly decreasing (Martin et al. 2016). All these observed changes mark a distinguishing point in history where the Arctic could be void of sea ice. This problem demands a thorough understanding beyond the old paradigm of the Arctic system as an unchanging seasonally forced region.

1.   Arctic Amplification

Cloud radiative forcing, ice-ocean albedo and Pacific-and-Atlantic origin warm current advection are a collection of feedback systems that enhances the Arctic's sensitivity to temperature increases associated with carbon-dioxide-driven global warming. The steady decline in late September sea ice extent through the late 1990s motivated the Surface Heat Budget of the Arctic (SHEBA) experiment to investigate how ocean properties within the ocean change to maintain an equilibrium for sea ice cover at all seasons of the year. Their results indicate the important role of cloud cover that changes the longwave radiation transport to and from the ice-atmosphere interface (Serreze and Barry 2011) and the enhancement of sea-ice melt or growth rate with ice-ocean albedo variation (Morrison et al. 1999) and Pacific-Atlantic warm-current advection (Maslowski et al. 2014).

a.   Cloud Radiative Forcing

Based on direct observations in the Arctic region, several greenhouse-gas-driven Global Circulation Model (GCM) simulations (Walsh and Chapman 1998) indicate a proportional relationship between cloud radiative forcing and the rate of net surface warming (Intrieri et al. 2002). Evidence collected during the SHEBA experiment shows the predominance of broken (5 to 7 oktas) to overcast (8 oktas) skies in the winter-spring produced a deficit of incoming shortwave radiation leading to surface ice warming due to solar energy reflecting back to the surface as longwave radiation as it attempts to pass through clouds (in-cloud trapped shortwave radiation). Additionally, the high snow/ice albedo and cloud covered conditions typical of Arctic winters accounted for elevated net radiative energy fluxes greater than the clear-sky and lower sea ice albedo in the summer. Accordingly, with the exception of the summer, cloud radiative processes in the Arctic trap heat compared with lower latitudes, due to differences in surface albedo and predominate

Arctic cloud cover. Arctic conditions effectively store the longwave radiation emitted from the surface and reradiate it back (Figure 4). In the lower latitudes, most of the incoming radiation is reflected back to the atmosphere to produce a net cooling effect in the absence of longwave cloud ice trapping (Curry and Ebert 1992). Complex cloud radiative processes at the atmosphere-ice interface are one of the processes leading to amplified responses to climate change in the Arctic. A framework level understanding of significant Arctic processes and their responsive feedbacks is essential to achieving cohesion between observations and modeling of prospective climate change in the Arctic region (Maslowski et al. 2012).
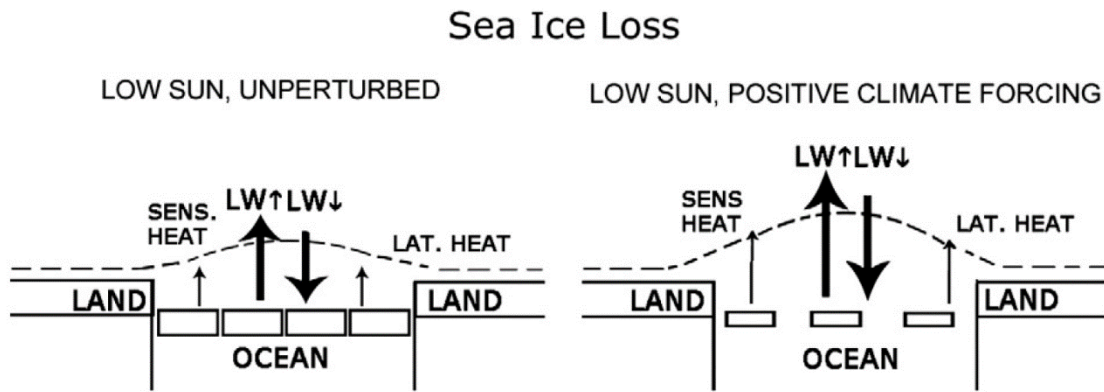
Display on the left represents a static Arctic. Display on the right represents the reaction to a warming climate. The dotted line is the lower troposphere isotherm. SW is shortwave radiation flux, LW is longwave radiation flux, Sens. Heat is sensible heat flux, Lat. Heat is latent heat flux.

Figure 4.   Arctic surface energy budget in response to changes in sun exposure. Source: Serreze et al. (2011).

b.   Ice-Ocean Albedo Feedback

Sea ice constitutes approximately 7–10% of world's oceans and covers ~4-6% of the Earth's surface, yet it has a large impact on the global climate disproportionate to its mass, which, particularly when coupled with wind forcing, makes the Arctic more sensitive to temperature variability than any other place on Earth (Wadhams 2003). On average, the Arctic Ocean reflects ~6% of incoming shortwave radiation and absorbs ~94%. Empirical data shows that a snow-covered Arctic reflects ~85% of incoming solar radiation and sea

ice reflects ~60% of all incoming solar radiation back into the atmosphere (Strum et al. 2002). The ice-ocean albedo feedback is based on the increasing absorption/decreasing reflection of incoming solar radiation that occurs through the summer as snow-covered ice melts to bare ice, which melts to open water. As the ice melts, open water fraction and solar radiation transmission through the bare ice and melt-ponds rapidly increase the flux of solar heat into the upper ocean. Shortwave radiation entering the ocean is absorbed rapidly in the upper 15m, where it contributes to basal ice melt near or formation of a near-surface temperature maximum if a dynamically isolated fresh melt layer has formed. Consequently, a significant removal of Arctic snow decreases the overall concentration of Arctic sea ice. This increases the probability of through-ice radiative intrusion that makes sunlight more available for ice-cover penetration and heating of the upper mixed layer (Gallaher et al. 2014). Based on two Community Earth System Model (CESM) simulations, the first using a 1% per year carbon dioxide run with standard sea ice cover and the second with the same carbon dioxide input, but with fixed Arctic sea ice cover. Seasonality and geographic area have direct influence on sea ice cover variability and feedback mechanism generation in a greenhouse gas induced warming environment (e.g., AA). As sea ice coverage diminishes, longwave radiation reflected back into the atmosphere increases, which leads to strong temperature gradient development between the overlying atmosphere and sea ice (~10-30 ºC). Subsequently, AA events primarily develop during the cold season as strong thermodynamic gradients produce stress on surface ice leading to divergence and latent release and sensible heat fluxes to the atmosphere. These phenomena intensify when coupled with preexisting atmospheric water vapor and other feedbacks (Taylor et al. 2013).

c.   *Pacific- and Atlantic-Origin Warm Current Advection*

Advection of warm Pacific and Atlantic water into the Canadian Basin is an important potential moderator of sea ice volume and extent. The distinct geographical influence of these thermodynamic driven currents requires an understanding of their climatological circulations (Maslowski et al. 2004). In the western Arctic during the summer, warm Pacific water flows through the Bering Strait and melts ice to the north into the Chukchi and Beaufort seas (Shaw et al. 2009). In the winter, the Pacific water cools and ice forms a boundary along the continental slope of the Chukchi Sea, separating the

shallow depths (~50 m) of the shelf region and deep waters of the Beaufort Sea. The shallow waters in the shelf region can be mixed down to form ice, but the deep waters of the Beaufort Sea (~3000 m) make it virtually impossible for ice to form due the longer requirement of mixing and cooling via wind forcing. By contrast, in the eastern Arctic during the winter, warm Atlantic waters, several degrees above freezing, split at the Norwegian Sea, one branch flowing between Norway and Svalbard through the Barents Sea opening, and the other through Fram strait as the West Svalbard Current (WSC). Both currents provide a constant influx of warm water available to melt ice through the winter, which contributes to setting the sea ice extent boundary (but not in the central Arctic where the Atlantic water subduct hundreds of meters down into the pycnocline). In the summer, the heat content of the Atlantic Ocean increases and melts more ice (Aagaard et al. 1987). As was the case of the Pacific warm water advection, the continuous flow pattern of the Atlantic warm waters restricts the seasonal extent of sea ice. Additionally, the tilt of the Earth's axis provides 24-hour sunlight exposure for maximum warming to melt more ice versus less warm water in the wintertime. These thermodynamic and dynamic processes prevent winter-time ice formation across Fram strait due to the WSC and determines the position of ice in the Barents Sea and the Greenland shelf. Not only is the sea ice developing in the winter season thinner, but it is weaker and has less volume. Almost all high-resolution model outputs, averaged and integrated over decadal timescales (Maslowski et al. 2004), forecast an increase in global warming (Hu et al. 2013) and ensuing continuing reduction of Arctic sea ice cover (Pedersen et al.2019). To that point, as of September 19, 2019, the NSIDC has estimated that Arctic sea ice extent is 4.3 million square kilometers (Figure 5), which is the lowest seasonal minimum extent in the satellite record since measurement began in 1979 (NSIDC 2019).
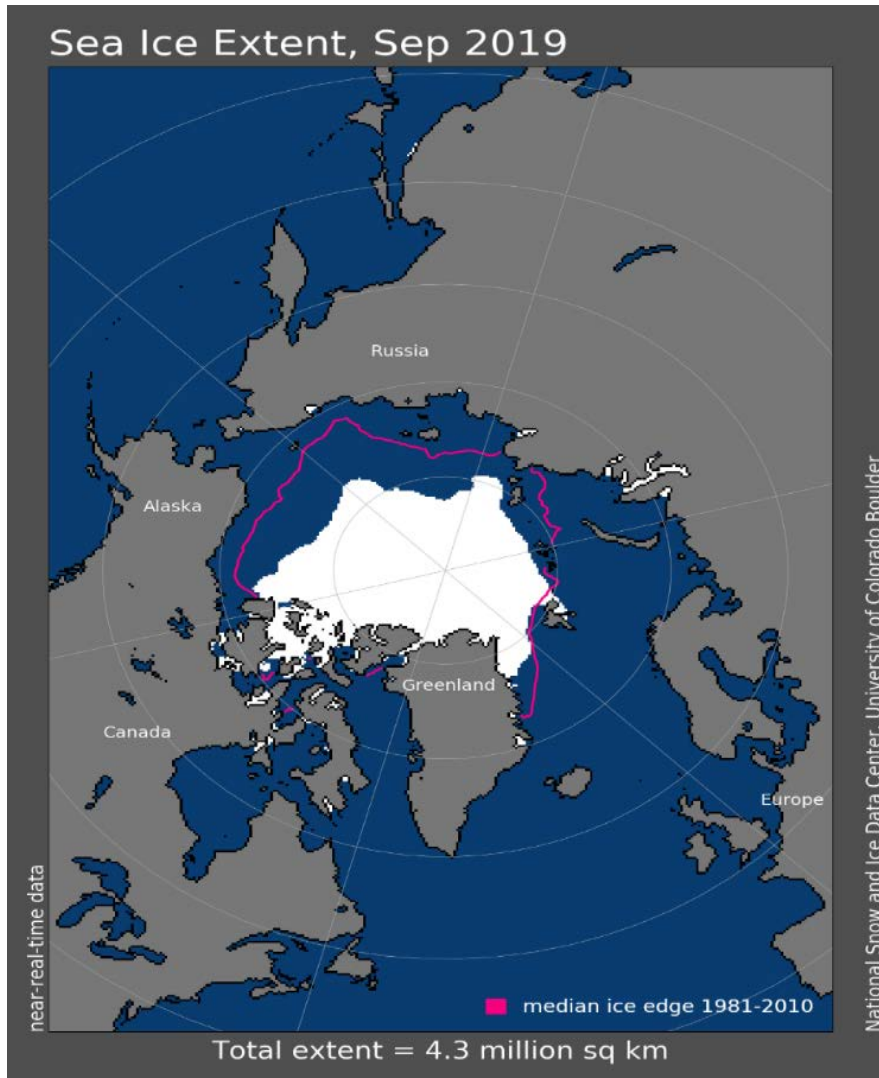
The pink line indicates the median ice edge. The white area is the observed sea ice extent.

Figure 5.   September minimum sea ice extent. Source: National Snow
and Ice Data Center (2019).

2.   A Review of Arctic Field Experiments

The Arctic Ice Dynamics Joint Experiment (AIDJEX) in 1975 was the first extensive western Arctic sea ice experiment to explore the effects of oceanic and atmospheric responses to sea ice movement. Through analysis of upper ocean development from four AIDJEX drift stations over the summer season, the notional layering of the upper water column was quantified. This is significant because the annual melt cycle and freshwater inputs influence an otherwise nearly unchanging salinity profile throughout the

year. River influx from neighboring continents coupled with snowmelt provide the mechanism for ice formation. Additionally, this layering forms a relatively shallow, cyclic freshwater layer above a well-developed pycnocline. Frozen in to a MYI floe and drifting nearly a year (1997–1998), from the middle of the Beaufort Sea to just over the Northwind Ridge (McPhee 2008), the SHEBA research team aboard the Coast Guard Icebreaker *Des Grosiellier* documented changes in available summer melt water and sea ice extent. Taking measurements spanning the mixed layer into the stratified part of the ocean, the SHEBA ocean profiler collected upper ocean temperature and salinity measurements with concurrent thermal microstructure measurements near the center of the Beaufort Gyre that indicated it was 10% fresher than samples collected during the AIDJEX in the same vicinity and season in 1975 (McPhee et al. 1998). This observed freshening of the mixed layer from ~30-45-meter depth was attributed to extreme melting from the previous summer season (McPhee et al. 2008). A primary effect of declining summer sea ice extent was the need to understand the evolving marginal ice zones in the Canada Basin. The 2014 Marginal Ice Zone experiment (MIZ), initiated and funded by the Office of Naval Research, investigated a range of dynamic, thermodynamic and wave processes controlling the late summer MIZ. Gallaher et al. 2014 found that the lack of outside oceanic influence (e.g., long period swells) and comparable wind forcing events between the observation period and the climatological mean suggest that thermodynamic processes control melt-back and the formation of a large area marginal ice zone in the Canada Basin. In response to longer periods of sun exposure, sea ice kinematics reduce sea ice cover, hence decreased ice albedo, which leads to increased absorption of solar radiation, greater warming and melt pond generation. Further sea ice melt coupled with the existence of melt-ponds leads to a decrease in ice strength/thickness, increase in ice drift and ice-ocean stress, and turbulent oceanic heat flux into the mixed layer. These sequence of events causes turbulent mixing through the ocean mixed layer to be limited by the formation of a fresher melt water layer just below the ice (Figure 6). The interplay between radiative input, accumulated surface (snow and ice) and basal melt and melt-pond generation was responsible for 50% of the total summer heat within the winter IOBL (Gallaher et al. 2016).
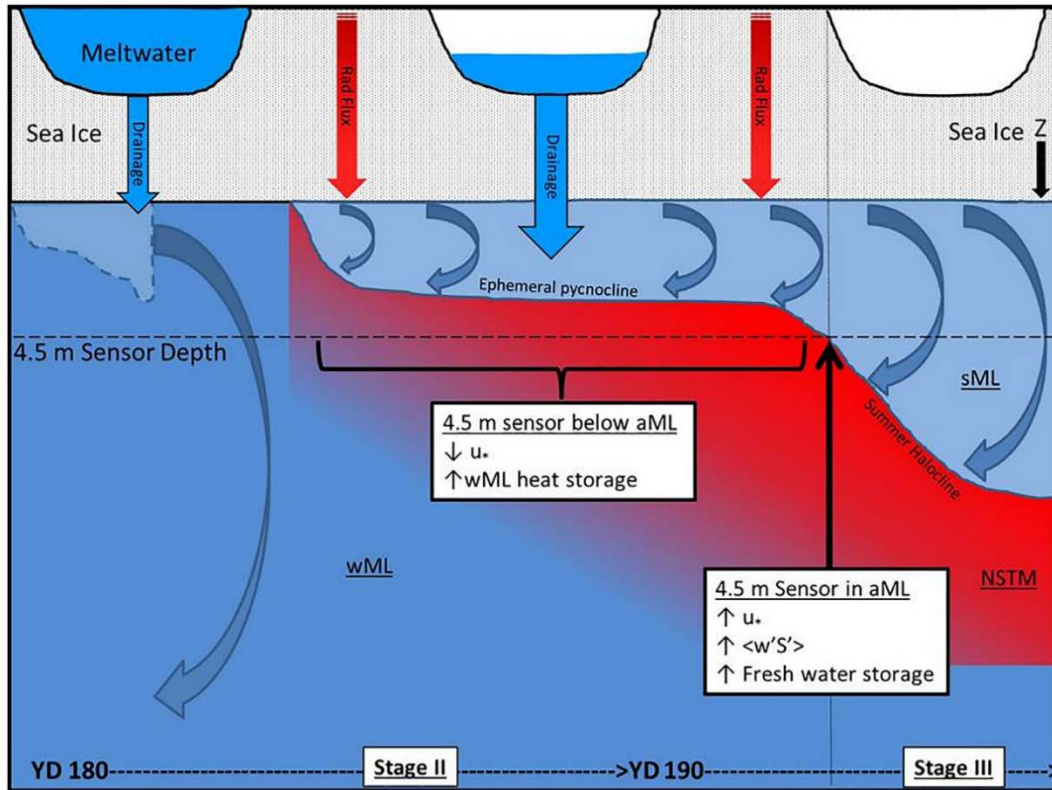
Figure 6.   Schematic demonstration of drained melt pond water influence on
the IOBL-OML within the sea ice and the upper ocean domain.
Source: Gallaher et al. (2016).

The 2014 MIZ Department of Research Initiative (MIZ DRI) effectively quantified the impact increased open water fraction had on sea ice evolution within the MIZ. The Office of Naval Research (ONR) motivated Stratified Ocean Dynamics of the Arctic DRI (SODA DRI) sought to evaluate how these changes regulate upper ocean stratification, circulation, and acoustic propagation within the Arctic and the effect on momentum and buoyancy transfer within the atmosphere-ice-ocean interface. Observations have been gathered throughout an annual cycle, and over an extensive latitudinal range (Lee et al. (2016).

3.   Physical Changes Associated with Decline of Arctic Sea Ice Cover

In neutral or weakly stratified conditions in the ocean surface layer vertical heat fluxes may be measured using eddy-correlation methods and Equation 1.1 (McPhee 2008)

$$Q = \rho_o C_p \overline{w'T'}, \tag{1.1}$$

where ρ_0 is the density of seawater and c_p is the specific heat of seawater. Ensemble averages of 15 minutes are typically used to estimate Q.

The eddy correlation technique estimates the strength of vertical heat transport as a result of turbulent eddy motion in the Ice Ocean Boundary Layer (IOBL), a logarithmic boundary layer where stress is independent of depth, and the Ekman layer where the influence of the Earth's rotation (Coriolis-dependency) is important. The breadth of the constant stress layer generally extends only a few meters below the ice-ocean interface, and while the Ekman layer extends down to the pycnocline, typically 40m (Figure 7).

The speed difference between sea ice and the upper ocean generates ice-ocean stress (τ) that produces turbulent flow within the IOBL. Tangential variation at the ice-ocean interface characterized by the velocity scale $u_* = ((u'w')^2 + (v'w')^2)^{1/4}$, in which $u'w'$ and $v'w'$ are the lateral Reynolds stress components of the nine-element Reynolds stress tensor. Because ice-ocean drag varies with the ice basal roughness, hydraulic roughness has contributions from small-scale features like ice scalloping to larger-scale features like ice floe edges, rafted ice, and deformed ice ridges. The ice-ocean drag coefficient can be expressed as $u_*^2 = c_d(u_{ice})$, where $c_d = \dfrac{u_*^2}{\sqrt{u_{ice} + v_{ice}}}$ is the ice-ocean drag coefficient and u_{ice} is the scalar ice velocity. The effective ice base roughness directly influences sea ice layer thickness, current variance with depth and rate of turning at the base of the IOBL (Cole et al. 2017).

It is this effect which makes the sea ice cover such an important component of Arctic change. Conclusions from the previous Arctic field experiments have explored different physical processes linking Arctic warming and ice pack melt-back. Thinner and weaker sea ice cover produces an environment in which heightened ice drift sensitivity to geostrophic forcing generate both thermodynamic and dynamic effects.
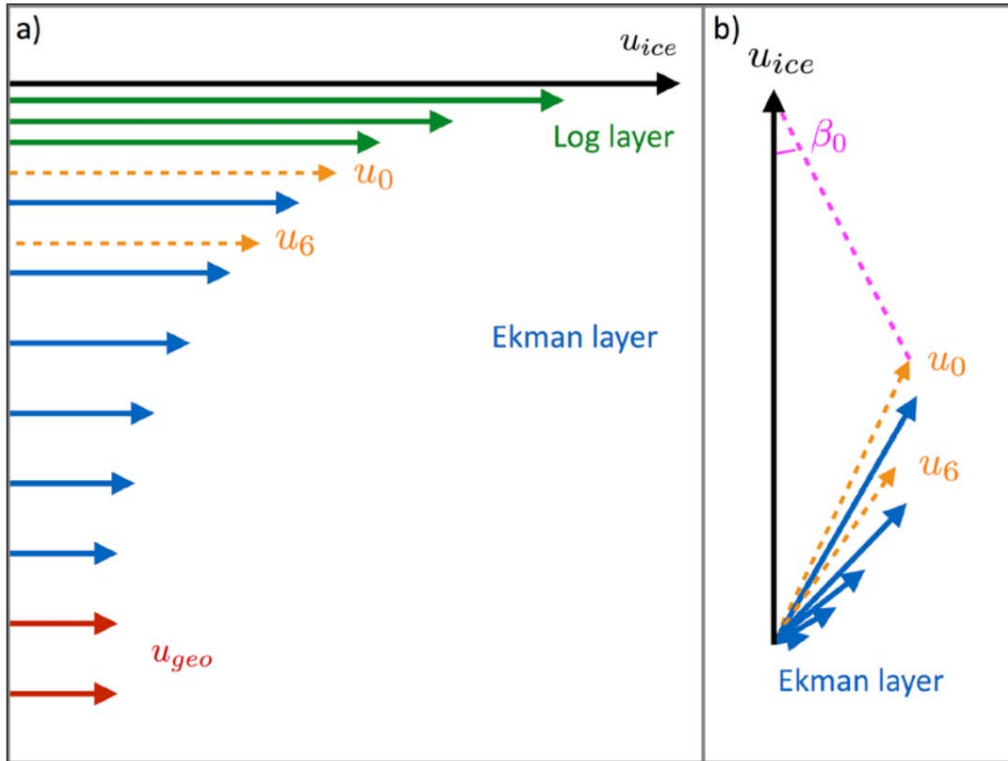
a) A hodograph view, and b) Black vector is the geostrophic current. (u0) is the velocity at the logarithmic boundary and Ekman layer interface. (u6) is a represents the measurement depth for winter conditions. β0 is the turning angle of the ice-ocean drag coefficient.

Figure 7.   Diagram of ice and upper ocean currents.
Source: Cole et al., (2017).

Because the magnitude of these effects are directionally dependent (anisotropic), sea ice moving at different speeds and directions relative to one another can cause the ice cover to shear and converge/diverge (Kwok 2001). These ice deformation events remove energy imparted into the ice and usually manifest in ridging and rafting during ice convergent conditions (Rigor et al. 2002) or lead formation in-divergent events (Dyne et al. 1992). The effect of energy dissipation associated with sea-ice movement modifies ice thickness distribution within the Arctic system. For example, ice divergent events in the winter add sea ice volume by re-freezing relatively linear open water features (leads) in the sea ice cover. The exposure area of a newly formed ice leads in contact with the atmosphere above significantly influences local ocean-atmosphere exchange (Dyne et al. 1992). In addition to how resistant sea ice is to wind forcing, its delivery of momentum throughout

14

the water column is also controlled by the top and bottom surface roughness (Martin et al. 2016). Ice-ocean drag coefficients for both the air-ice and water-ice interfaces are a function of ice hydraulic roughness and stability of near-surface stratification (Martin et al. 2016). Surface roughness of the ice affects atmospheric drag, while form drag produced by large features, like the edges of ice type features (leads, melt ponds, and floes), and underside roughness affect near-surface transport of energy and momentum (Lupkes et al. 2013). The ONR Marginal Ice Zone experiment in 2014 studied these processes by deploying several drifting instrument clusters (C2, C3, C4 and C5) in the eastern Canada Basin to observe different component changes at the atmosphere- ice-ocean interface. Velocity measurements between the log and Ekman layer (u_0) and observations ~4.5 m (AOFB) and ~6.5 m (ITP-V) below the ice surface were used to measure the local fraction turbulent velocity u_*. The corresponding turning angles ($\beta_0, \beta_4 \, and \, \beta_6$) of the ice-ocean drag coefficient estimates ($c_{d_0}, c_{d_4}, c_{d_6}$), derived from turbulence observations near the top of the Ekman layer (Figure 8) documented a seasonal correlation between increased under-ice roughness and higher ice-ocean drag coefficients (Cole et al. 2017). This was characterized by the Ekman (15-30 m) and log layer (0.7–1.5 m) depths shallow enough to fit inside the seasonal mixed layer.

The average ice draft (2-m) calculated from drifting IMBs over a 5-km scale at each cluster and a 1.5-m log-layer estimated from daily mean Ekman depth measurements, produced estimated surface Ekman layers (3.5-m depth) well above the 8m depth of the ITP stress measure. The depth of the log layer was estimated using the daily mean Ekman depth and was supported by homogeneity between the log and Ekman layers friction velocities at cluster C2. Consequently, each cluster experienced different ice-ocean drag coefficients based on season, deployment location and underlying ocean characteristics. Deployed on a MYI floe, cluster C2 experienced the largest ice-ocean drag coefficients and roughness length decreases early in the study period (March) due to basal melting and decline in pack ice concentration (Cole et al.2017).

15
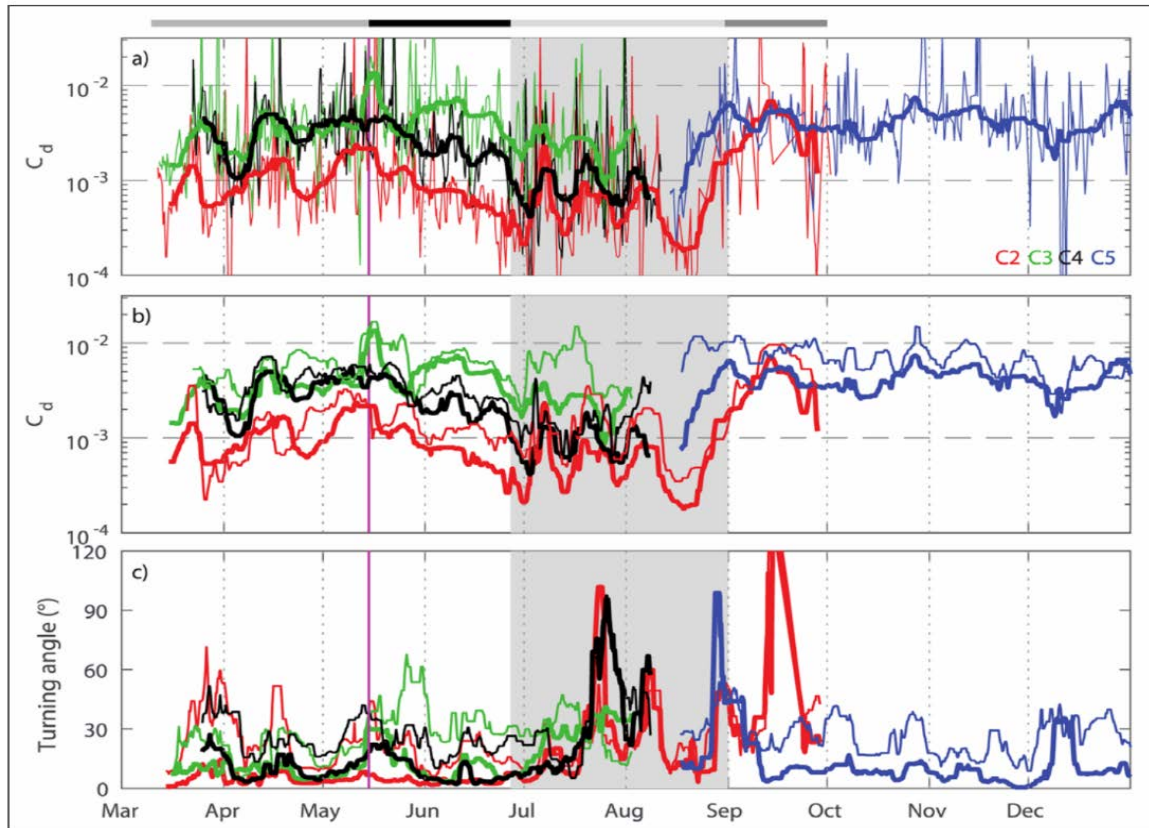
a) Ice-ocean drag coefficient at 6m depth with weekly median in gray, b) weekly median ice-ocean drag coefficient at 6m (Cd6) and surface depth (Cd0) values, and c) weekly median of 6m (β6 (thick)) and surface (β0 (thin)) turning angle estimates.

Figure 8.   Ice-ocean drag coefficient and turning angle estimates at C2–C5. Source: Cole et al., (2017).

4.   Naval Mission Objectives in the Arctic

a.   *ONR Marginal Ice Zone (MIZ) Program*

Of all the missions the U.S. Navy has engaged in, the Arctic region presents unique challenges. Sea warming associated with sea level rise from glacial melt in Greenland and Antarctica, coupled with perennial ice pack changes in the Arctic are but a few factors contributing to an increase in USN responsibility. The Navy Office of Naval Research and the USN are working with global partners to measure Arctic changes and quantify the impact to Naval operations. Notwithstanding the cessation of the Navy's Task Force Climate Change initiative, a strategy introduced in 2009 with the key objective of

improving the cross-sectoral integration of future public perspective and U.S. strategic policy on the issue of climate change, the Navy's mission outlined in the USN Arctic Road Map remains the same: 1) gather a better physical understanding of Arctic dynamical processes to support freedom of navigation, 2) develop better ways of observing the Arctic to defend the homeland and contribute to maritime domain awareness, and 3) incorporate collected data into an accurate prediction system. The USN's invested interest in Arctic research is evidenced through several Department Research Initiatives (DRIs). The MIZ project described in earlier sections, the Arctic Sea-State air-sea interaction project, and most recently the Stratified Ocean Dynamics in the Arctic project (SODA). The Office of Naval Research (ONR) motivated SODA project seeks to evaluate how changes in the upper Arctic waters regulate ocean stratification and circulation within the Arctic and the effect on momentum and buoyancy transfer within the atmosphere-ice-ocean interface (Figure 9). Observations are gathered throughout the entire year cycle in the Canada Basin (Lee et al. (2016) and is providing a comprehensive data set of upper ocean processes. This thesis research draws on data collected from the SODA DRI.
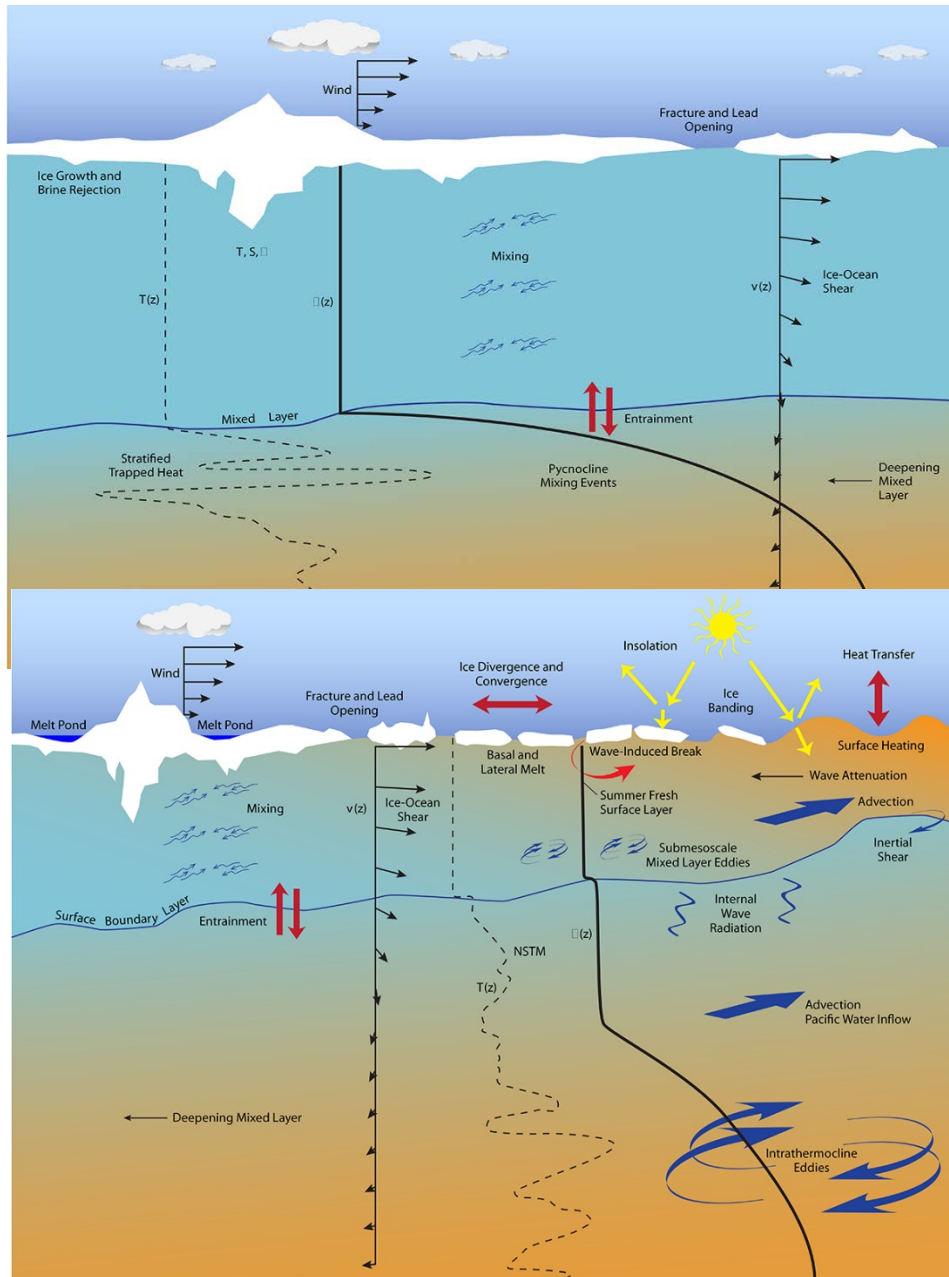
Figure 9. Schematic show (top) the winter and (bottom) summer processes that control upper ocean stratification and sea ice evolution in the MIZ. Source: Lee et al., (2016).

II. SAR AND IMAGE PROCESSING BACKGROUND AND CONCEPTS

Sections A provides an overview of Synthetic Aperture Radar imaging techniques. Section B summarizes image processing concepts used in this thesis project.

A. SAR IMAGERY

1. SAR Background

Air defense and over-the-horizon surveillance strategies during World War II provided the framework for technological advances in the employment of remote sensing systems. The invention of Radio Detection and Ranging (radar) by German inventor and energy (backscatter) back to the receiving SAR sensor. As shown in Equation 1.2, the surface area viewed by a SAR is based on sensor altitude and surface area at a specific moment in time.

$$S \approx \frac{\lambda}{L} R \equiv \beta \times R[m],\qquad(1.2)$$

where S is the size of the instantaneous footprint of the along-track footprint, R is the distance the radar sensor is from the ground, L is the side length of the antenna (specifies the antenna's beam width $\beta = \frac{\lambda}{R}$ where λ is the generated wavelength and the lateral distance of the antenna. SLAR systems sort the returned satellite echoes in both range and azimuth direction, while signals backscattered from the ground arrive back to the satellite sensor at different times based on its location within the swath, and can only be distinguished if the range R difference is greater than half the transmitted pulse length (range resolution) as defined in Equation 1.3.

$$\rho_R = \frac{c \times \tau_p}{2}[m],\qquad(1.3)$$

where ρ is the range resolution in meters, c is the speed of light and τ_p is the pulse length.

The object of remote sensing systems is, as accurately as possible, to discriminate between objects on the ground. This contrasts them from SLAR systems, in that their ability to distinguish between targets in the azimuth direction depends on the width of the azimuth footprint *S* and is restricted by the side length *L*. This limitation degrades the azimuth resolution (approximately equal to the instantaneous footprint) with increasing range R, and makes the application of SLAR systems on space-borne platforms unfeasible, based on the pulse length's reliance on distance to the ground.

2.   SAR Basic Concepts

In 1952, a Good-year Aircraft Cooperation engineer, named Carl Wiley (Cumming and Wong 2005) discovered a connection between the lengthways-trace coordinate relative to a transmitted radar beam of a backscattered object, and the instantaneous doppler shift of the signal backscattered to the radar by that object. He hypothesized that the frequency of satellite signals could improve spatial resolution along the track of the satellite beyond traditional SLAR systems. Wiley's concept, "aperture synthesis" capitalized on the relationship between the antenna length *L* and radar resolution (Figure 10). This process magnified the radar resolution by integrating multiple shorter antennas, in order to increase the antenna length that serves as the foundation for all modern radar systems.
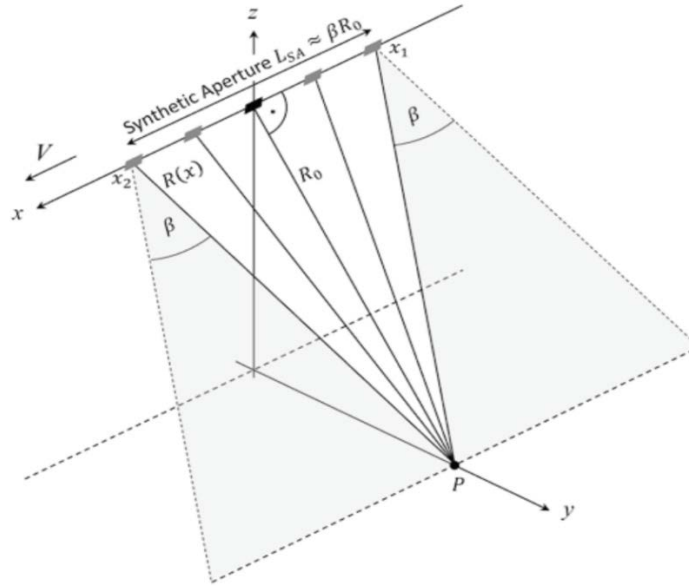
Figure 10.   Synthetic aperture for target P along track. Source: Meyer (2018).

a.   *Geometric Property Considerations associated with SAR imaging systems*

SAR operates at a swath width between 30 and 500 km, with spatial resolutions between 1 to 200 m. This makes it ideal for observing local and regional ice property changes that distinguish the condition of the sea ice cover. The SAR's looking angle (θ) and sloping angle to the underlying surface (α) influences how the SAR image will appear. For example, foreshortening, layover and shadowing are common geometric distortions in side-looking view configured SAR systems (Figure 11). In foreshortening, small looking and slope angles cause objects to appear closer than they really are. In layover, when the looking and slope angles are equal, backscatter from sloping surface on the ground are unevenly distributed and cause top and bottom features to appear disjointed. Although the effects of foreshortening and layover can be minimized by increasing the looking angle, larger looking angles do create shadow zones that obscure objects from the sensor's view.
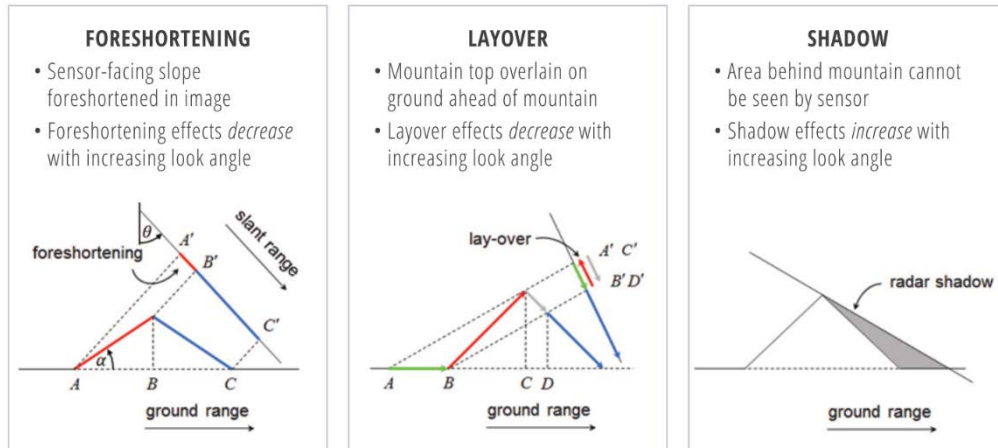
Figure 11.   Primary geometric distortions on SAR images.
Source: Meyer (2018

b.   *Radiometric Property Considerations Associated with SAR Imaging Systems*

The Arctic icepack consists of sea ice in many types and stages of development (Dierking 2013). SAR imaging systems are capable of identifying some physical properties based on the return intensity of the four different transmit / receive polarizations (Zhang and Skjetne 2018). Received signals are processed into geo-located two-dimensional (2-D) matrices. Each paired row and column are represented by an element called a pixel, which stores intensity values, typically as unsigned 8- or 16-bit values. The angle between the incoming microwave pulse, the ice surface (incident angle) and polarization projected by the SAR determines the brightness sea ice exhibits in a given pixel. Changes between neighboring cells through a SAR image are the result of the amplitude and phase variation from pixel to pixel, leading to the granular (speckle) appearance characteristic to SAR imagery (Figure 12).

Figure 12.   Sample space-borne SAR dataset acquired by
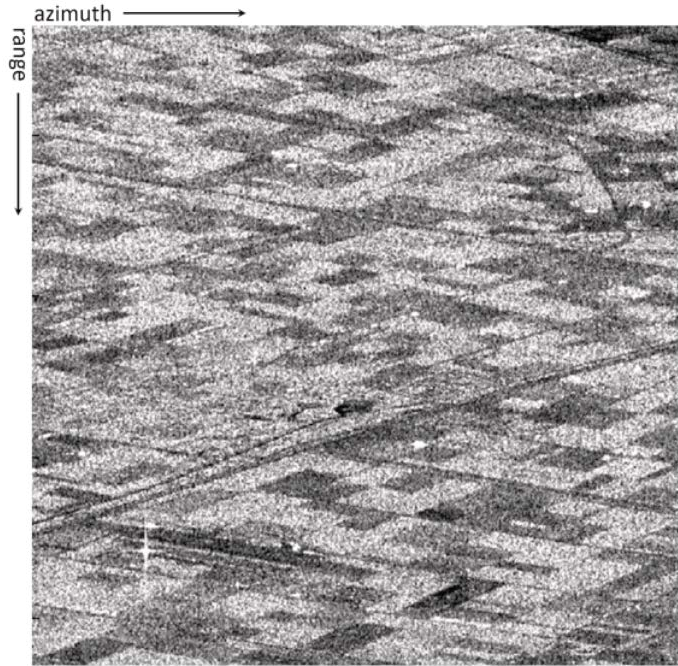ESA's C-band sensor ERS-2. Source: Meyer (2018).

The distribution of signal scattering within each pixel depends largely on the dielectric properties of the ground scatterers. Accordingly, in summer, as open water fraction increases, open water produces low SAR backscatter levels. During the late fall-early winter, snow concentration on the surface of growing sea ice causes higher backscatter compared with ice without snow. Increasing sea ice cover and strong winds also contribute to changes in surface roughness, resulting in higher backscatter values. Typical radar frequencies used in satellite supported SRA systems are in wavelength/frequency divisions covering L-band (15-30 cm, 1–2 GHz), C-band (3.8-7.5 cm, 4–8 GHz), X-band (2.4-3.8 cm, 8–12.5 GHz) and Ku-band (1.7-2.4 cm, 12.5-18 GHz). Radarsat-2 and Sentinel-1 satellite data used in this research employ C-band signals to characterize the environment (Figure 13). The C-band wavelength is ideal for monitoring ice deformation signatures associated with lead and ridge formation due to its strong backscatter from rough surfaces at short wavelengths (~5.66 cm) and penetration capabilities.

BAND	FREQUENCY		WAVELENGTH		TYPICAL APPLICATION
Ka	27 – 40	GHz	1.1 – 0.8	cm	Rarely used for SAR (airport surveillance)
K	18 – 27	GHz	1.7 – 1.1	cm	Rarely used (H_2O absorption)
Ku	12 – 18	GHz	2.4 – 1.7	cm	Rarely used for SAR (satellite altimetry)
X	8 – 12	GHz	3.8 – 2.4	cm	High-resolution SAR (urban monitoring; ice and snow, little penetration into vegetation cover; fast coherence decay in vegetated areas)
C	4 – 8	GHz	7.5 – 3.8	cm	SAR workhorse (global mapping; change detection; monitor-ing of areas with low to moderate vegetation; improved pen-etration; higher coherence); Ice, ocean, maritime navigation
S	2 – 4	GHz	15 – 7.5	cm	Little but increasing use for SAR-based Earth observation; agriculture monitoring (NISAR will carry an S-band channel; expands C-band applications to higher vegetation density)
L	1 – 2	GHz	30 – 15	cm	Medium resolution SAR (Geophysical monitoring; biomass and vegetation mapping; high penetration; InSAR)
P	0.3 – 1	GHz	100 – 30	cm	Biomass. First P-band spaceborne SAR will be launched ~2020; vegetation mapping and assessment. Experimental SAR.

Figure 13.   Microwave bands designations. SAR systems generally utilize the frequency bands in green. Source: Meyer (2018).

B.   IMAGE PROCESSING

1.   Image Processing Background

Over the past 15 years, the extensive accessibility of low-cost hardware and a wide range of software tools for image manipulation and processing, has made the extraction of information from digital images easier for content interpretation (Marques 2011). Numerous computer techniques for retrieving and inspecting data from images have been developed, and at times serve as a substitute for human visual interpretation. Image processing has emerged as a viable application within computer science spanning many human fields of activity. For example, within the medical occupation, imaging techniques associated with computerized axial tomography scans produce three-dimensional (3D) images of the brain's composition and structure from an assortment of large series 2-D X-ray images (Seletchi and Duliu 2006). For years, for law enforcement and military, cameras modified with range finders (range cameras) and radars with radiative detection capabilities (forward-looking infrared radar) have provided a critical advantage, from troop and vehicle movement detection to intelligence gathering operations and target recognition (Marques 2011). In the Arctic, advances in characterizing ice parameters have included ice concentration calculation, sea ice classification and ice floe identification. For example,

the intensity variations across a 2-D scene of the ice pack generally exhibits higher intensity (brighter) values than water. Subsequently, using threshold methods (Markus and Dokken 2002) or the application of sea ice concentration algorithms on European Remote Sensing (ERS) to SAR images (Johannessen et al. 2013) allows ice concentration estimation. Classification of ice types in SAR images through cluster analysis and labeling, using lookup tables to quantify varying ice types based on backscatter signatures, has also demonstrated a viable means of distinguishing between MYI and First-Year Ice (FYI) boundaries (Kwok et al. 1992).

2. Image Processing Concepts and Terminology

a. Image Types

An image consists of an endless number of 3-D projections that are conformed to a 2-D visual representation of a scene (e.g., an object, bird or person) captured by an ocular device (e.g., radiometer, camera, or lens). Each pixel, within a monochrome (grayscale) image, has an associated numerical value constituting the intensity of the pixel, normally in a (0, 255) 8-bit, or (0, 65535) 16-bit range. The nominal structure for grayscale images typically have 8 bits per pixel construction where pixel values of 0 corresponds to "black," and a pixel value of 255 corresponds to "white," and values in between indicate varying shades of gray (Figure 14). Images that are composed of two discrete pixel options (1 or 0) are called binary images. Based on analysis requirements, intensity images have a variety of data class options to display in the Matrix laboratory (MATLAB) software. Grayscale images used in this research are composed of integers (uint8 and uint16) to represent pixel intensity. These images are called indexed images and are composed of a matrix of integers and a color map. Unsigned integers (uint), where u stands for unsigned (all positive values), and int means integers (whole numbers), represent a wide range of intensity values. Images can also be represented as double precision numbers within MATLAB allowing MATLAB arithmetic functions to be applied.
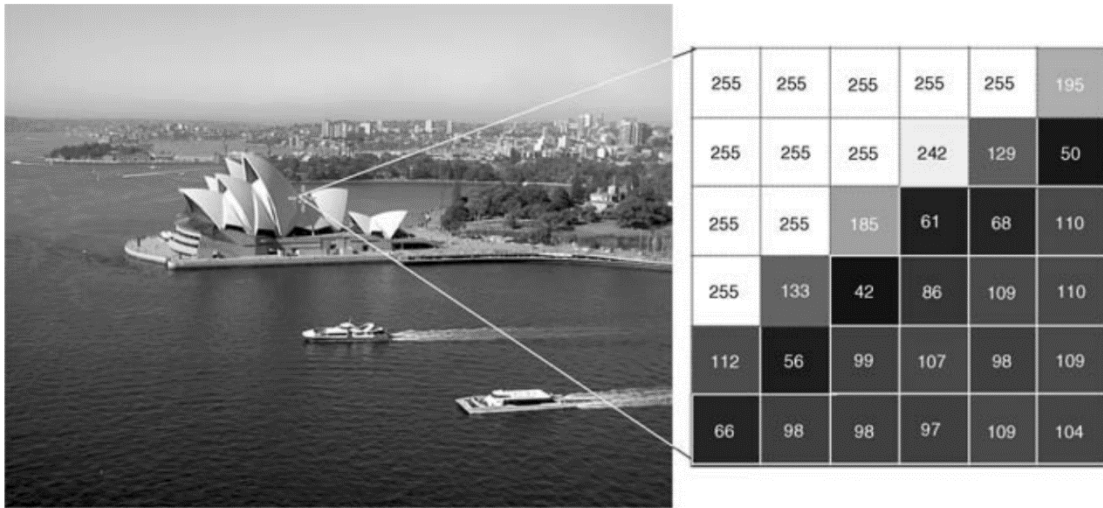
Figure 14.   Grayscale image with a 6 × 6 matrix of large
numerical value pixel representing higher intensity pixels.

b.   *Basic Relationship between pixels*

Feature analysis of images can exploit the relationship between pixels in smaller matrices of similar value. For example, a 4 and 8-neighbors' construction are two common image processing operations that reveal how pixels are connected vertically and horizontally to a reference pixel (Figure 15). A 4-neighbor pixel matrix identifies and groups a pixel's position based on a four-sided contact aspect (above, below, right, and left) of a reference pixel (p) in the image. The manner in which pixels are connected to (p), whether diagonal, vertical or horizontal, can be used to reduce the image pixel variance from true intensities of the real world (de-noise), estimate pixel intensities at unknown locations based on known pixel intensities (interpolation), and partition an image into regions (segmentation), to name a few. As a result, a set of intensity values at one location can be used as a gauge of similarity for adjacent pixels (adjacency). For instance, two pixels can be viewed as either a 4 or 8-adjacent matrix if there are an equivalent number of neighboring pixels of the same formation scheme. A mixed adjacency process can be applied to supplement inherent ambiguities (e.g., redundant paths) associated with 8-adjacency. The intrinsic path between two pixels (p and q) is a series of pixel operations, always starting with the pixel labeled as p and ending with the pixel labeled as q. A 4 or 8-

26

path construct implies that number of connected pixels and are called a component, which can be placed into related data groups called structure arrays.
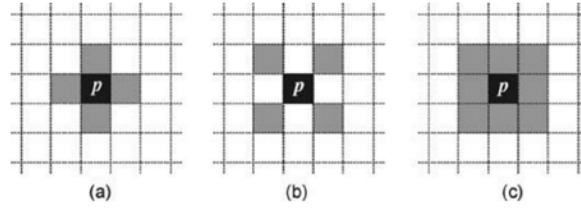

Figure 15.   Schematic of neighborhood of pixel *p*: (a) 4-neighborhood; (b) diagonal neighborhood; (c) 8-neighborhood. Source: Marques (2011).

THIS PAGE INTENTIONALLY LEFT BLANK

III. DATA COLLECTION AND METHODS

This thesis will utilize data collected from the Naval Postgraduate School (NPS) AOFB 41 and AOFB 42 data sets, Woods Hole Oceanographic Institute (WHOI) ITPs, and Sentinel 1A medium-resolution (MR) Extra-wide Swath Mode (EW) and RADARSAT-2 ScanSAR Wide Swath Mode (SCWA) SAR imagery collected from several sources by the Ocean Physics Department at the Applied Physics Laboratory-University of Washington. Data for both buoys were collected on a drift trajectory beginning in the Beaufort Seas and terminating ~350 nautical miles west of the Canadian Arctic Archipelago's Ellef Ringnes Island, with AOFB 41 terminating ~50 nautical miles to the northeast of AOFB 42 (Figure 16).
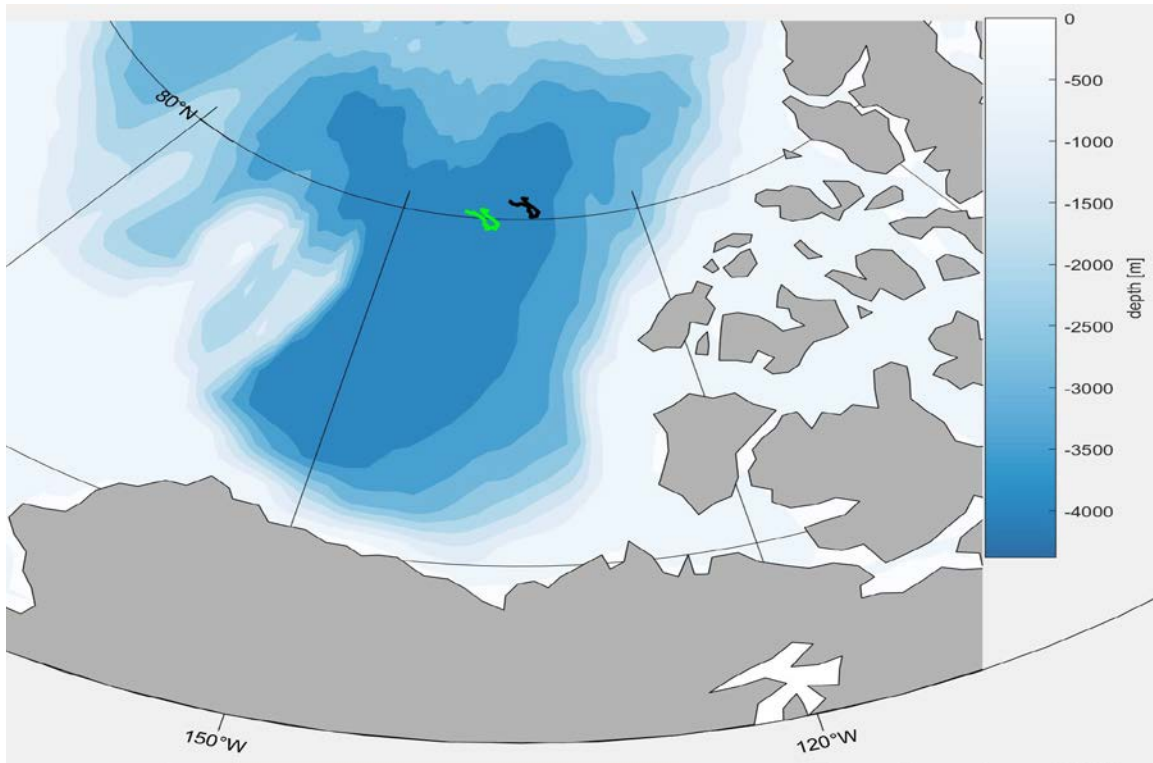

Figure 16.   Schematic of NPS AOFB track trajectories for buoys 41and 42 used in this research. Source: NPS AOFB (2019).

Sentinel 1A SAR and RADARSAT-2 imagery are unclassified, free and approved for public release through open data policy adopted by the European Union for the Copernicus program and the Government of Canada, respectively (European Space Agency (ESA 2019), Government of Canada). Image processing techniques are employed in this analysis to quantify OWF area, OWF area perimeter, and ice ridge length count surrounding each buoy at the time of each image.

The SAR images are transformed from geographic coordinates and presented in the polar stereographic projection to easting and westing coordinates, where the origin is at the pole, the + X axis is along +90 longitude, the +Y axis is along + 180, and the units are measured in meters.

A.   AUTONOMOUS OCEAN FLUX BUOYS (AOFB)

The AOFB is a custom-built instrument system constructed within the Ocean Turbulence Department at the NPS and designed to measure turbulent fluxes within the Arctic mixed layer just below the ice-ocean interface. Under both NSF and ONR funding, the NPS AOFB program deploys buoys from drifting ice floes to gather long time series observations within the ice-ocean interface over annual cycles. In 2018, two AOFBs were deployed in the Beaufort Sea (NPS AOFB 41 & 42) during the SODA project. AOFB consists of two main parts: 1) a surface buoy that rests on the ice surface that provides power to and gathers data from a range of instruments on the buoy including GPS position, meteorology measurements, current profile measurements and the turbulent flux sensor package. All data are recorded then sent by Iridium satellite link to a server at NPS. An instrument frame suspend from the surface buoy at 2m below the ice supports the ADCP, turbulent flux package and upward-looking altimeter to measure ice growth and melt. Two-way communication between the buoy and the NPS network takes place two times per day. This ensures near real-time data update stake place, and to remotely modify sampling schemes each instrument to conserve power and troubleshoot specific issues. The custom-built flux package includes an NPS-designed acoustic travel-time 3D current sensor with an inertial motion unit, an inductive conductivity cell and platinum resistance thermometer, and a fast response thermistor (Stanton et al. 2011, Shaw et al. 2008). The flux package

sensor suite measures dynamic and thermodynamic ocean processes (momentum, heat, and salt fluxes) using a direct eddy correlation technique which resolves the small turbulent fluxuations (u', v' and w') that arise from the turbulent eddy circulations in an inertial subrange. For more information visit http://www.oc.nps.navy.mil/stanton/fluxbuoy

B.   ICE-TETHERED PROFILERS (ITPS)

ITPs, developed by the WHOI usually accompany the NPS AOFBs on the same ice floes (Figure 17). As an autonomous system designed to measure upper ocean temperature and salinity profiles, ITPs add oceanographic value with an ability to profile the upper ocean for up to three years (WHOI 2007). Above the surface, the ITP instrument suite sits on the ice floe and consist of a power supply pack, iridium satellite and antennae for near-real time data transfer to WHOI and GPS unit (WHOI 2007). The surface suite also supports a plastic-jacketed wire rope tether that extends through the ice to 800m. The subsurface package contains a low power Conductivity, Temperature, Depth sensor with an associated mechanical wire track apparatus to move the profiler vertically along the tether.
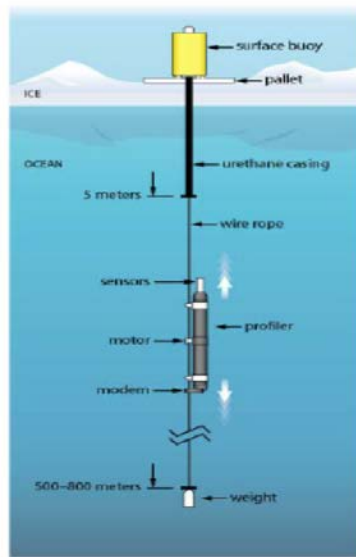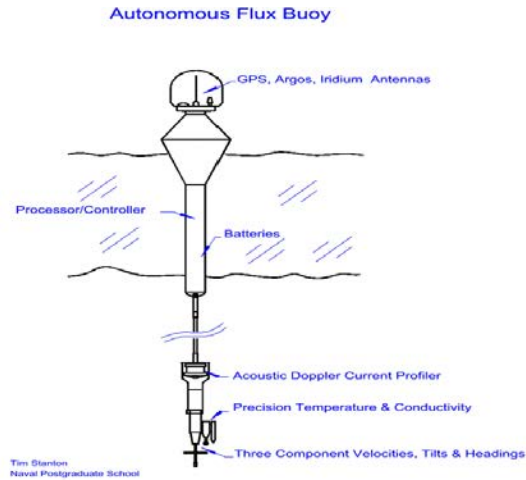
Figure 17.   Schematic of WHOI ITP and NPS AOFB. Source:
                  WHOI ITP and NPS AOFB. (2019).

1.   AOFB and ITP Association

Due to failure of the GPS receiver on AOFB41, in this study, data from the ITP104 and ITP105 position date (GPS) were used for the purpose of deriving polar stereographic x and y position data to calculate ice velocity (Figure 18). Data from the SAR images, AOFB and ITP were time-matched using their common GPS time stamps for each data set.
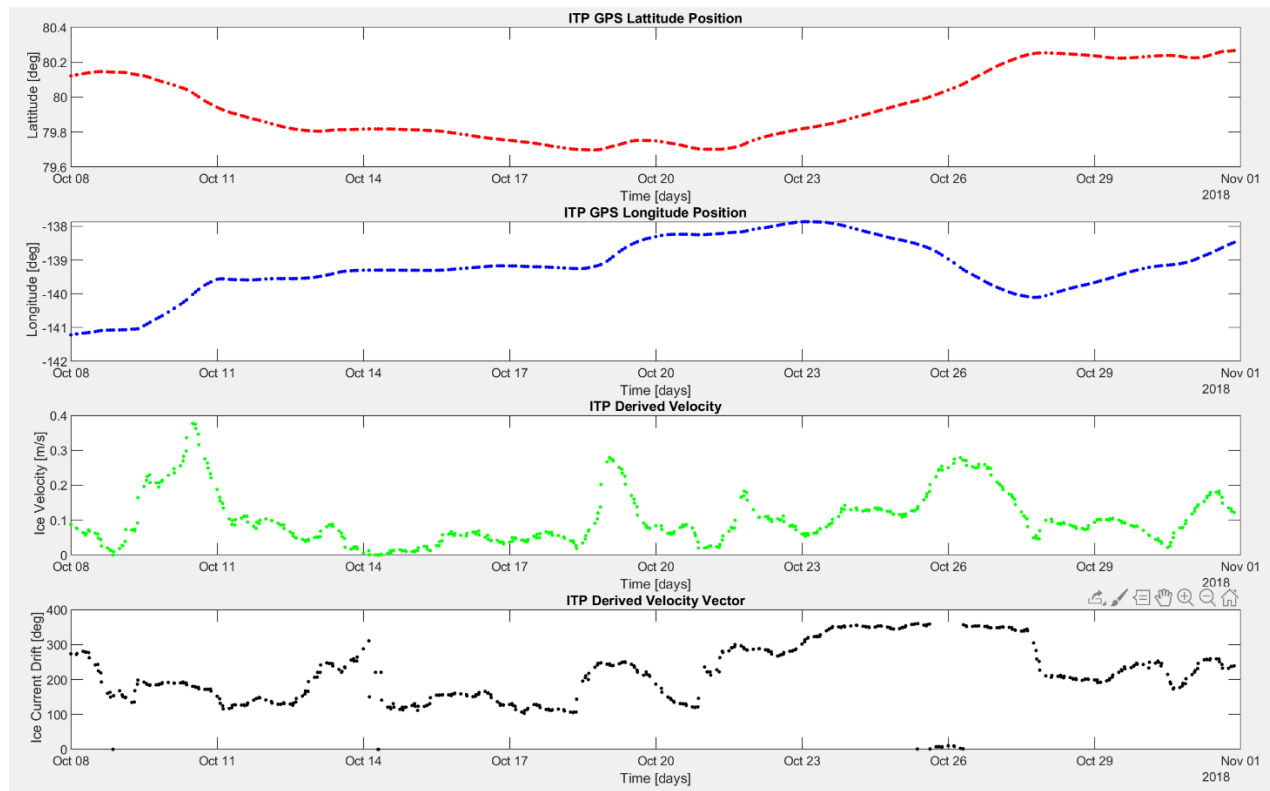
Figure 18.   Example AOFB GPS and derived ice velocity and vector

33

C.   SEA ICE IMAGE PROCESSING APPLICATION

1.   Image Processing Methods

This research utilized MATLAB code written to perform image processing techniques on medium-resolution satellite images coincident with AOFB trajectories. Pixel thresholds were selected for each image to produce OWF area, and joined pixel methods used to estimate OWF area perimeter values and ice ridge length. MATLAB functions and scripts were used to process the image data, using functions from the MATLAB Image Processing Toolbox, MATLAB website, and the NPS Turbulence Group processing toolbox. SAR images gathered together by the Applied Laboratory at the University of Washington were stored onto the NPS Turbulence server. Metadata files for each image were utilized to extract relevant image data to select appropriate images based on the time stamp of the image coincident to the closest buoy position. This procedure identified 82 satellite images that covered either AOFB41 or 42 locations, or "hit" images. Selected images were sub-sampled to 20-by-20 km centered on the buoy position at the time the SAR image was recoded and stored along with full resolution easting and westing positions of every pixel. The primary disqualifying criterion for image selection was that images were within ±6 hours of each AOFB and ITP time sync. A "hit" index was created from image metadata to look for all matching SAR occurrences based on current buoy number position. The closest AOFB time to the image time was used to select extract 2m depth friction velocity, ice velocity and 3m current from the AOFB instruments and stored into a data structure for further analysis. Image and buoy positions were converted to meters (easting and westing). Each of the stored zoomed in images was first retrieved in a program that displayed the pixel histogram in order to select appropriate threshold values for the open water / ice boundaries, and the few very bright ice ridge length features. Two programs were used to select and produce zoomed in 20x20 km sub images. The stored sub-images were retrieved in the feature analysis program. Before each sub-image is sectored for upstream feature analysis, the 20x20 km SAR images are loaded into MATLAB for pixel distribution analysis.

2. Determining OWF Area, OWF Area Perimeter, and Ridge Length Features

The aim of applying intensity-based image segmentation and edge detection algorithms is to identify OWF area, OWF area perimeter, and ice ridge length SAR images in the vicinity of a given buoy location. Ice ridges are made from ice fragments that subduct, buckle and break, then aggregate under the influence of strong wind forcing. The resulting ice convergence produces cracks, ice keels and ice ridges. These protrusions above and below the ice surface significantly increase the hydrodynamic roughness of the ocean/ice and ice / atmosphere boundary layers. Open water areas including leads (typically long open water features that form as cracks widen) form important paths for heat energy from the ocean in the winter (Dyne et al. 1992, McPhee and Stanton,1996) and paths for strong solar heating in the summer (Gallagher et al. 2014). The role of local open water areas in changing the local ocean-ice drag coefficient is investigated here by comparing the open water statistics of Radarsat-2 and Sentinel-1's SAR images with ocean-ice drag coefficients derived from the current strength and turbulent friction velocity measured by the SODA AOFB's. To accomplish this, image properties were analyzed and sectored into +-20-degree sectors directed upstream of the AOFB location at the time of the SAR image. These sectors were divided into image masks with six radial range bins of 0–500m, 500–1000m, 1000–2000m, 4000–8000m, 8000–16000m from the AOFB position.

The selected SAR images represented as a 2-D array are used to extract information about sea ice properties at the Arctic ocean-ice interface. Pixel value thresholds for the dark areas representing open water, and bright features representing ice ridges guided by pixel value histograms. The perimeter of open water features was determined using image analysis algorithms that utilize pixel neighborhoods and connectivity, and object-based operations within the MATLAB function "edge." Selecting an appropriate threshold range is a critical step in defining features within a SAR image and selecting pixel values outside the range of the ice features of choice will decrease the visible contrast within the image to isolate those features. The process of determining threshold values for each image consisted of reviewing the original SAR image and its associated histogram

a.   *OWF Area Threshold Determination*

The 20x20 km SAR image centered on the buoy location is used to locate low pixel intensity pixels within the image along with the histogram distribution which should rest significantly less that the images median intensity value. After reviewing the SAR image and histogram, a pixel threshold value is selected that reveals the open water areas seen in the raw SAR image in a binary mask image (Figure 19).
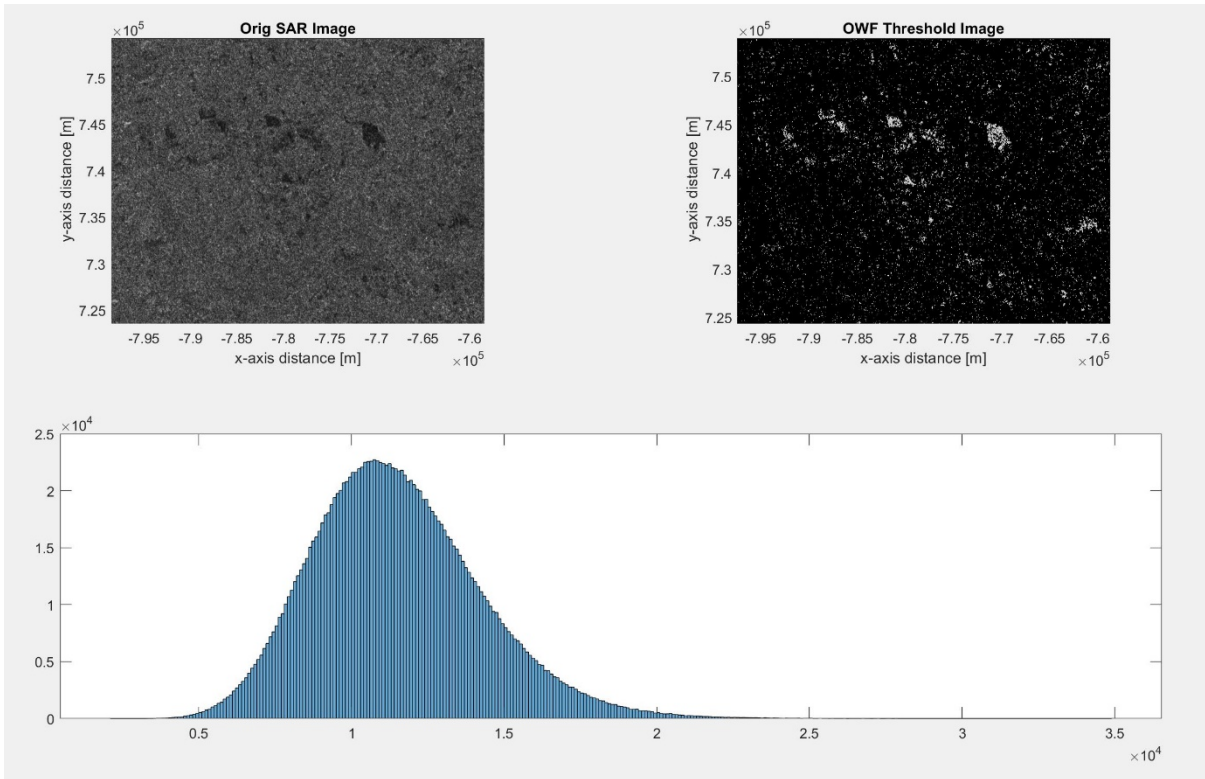

Figure 19.   Schematic outlining OWF area threshold determination process.

b.   *OWF Area Perimeter Threshold Determination*

Open water area perimeter is measured for each feature using image analysis algorithms that utilize pixel neighborhoods and connectivity, and object-based operations within the MATLAB function edge. The edge detection function in MATLAB calculates the change in pixel intensity between regions, by calculating the first derivative across the

intensity profile of the image. The use of the first derivative directly characterizes the difference in intensity across the ice-water boundary, thus detecting the presence of edges within the image for processing and analysis. There are primarily five widely known image detection algorithms (Roberts, Sobel, Prewitt, Robinson and Canny) of which vary, mainly by the masking technique each employs (Burnham et al. 1998). In this study, the Canny method was chosen because, unlike the others, it calculates the greatest maximum pixel value change (gradient) using a 2-D smoothing scheme (Gaussian filter) with a predefined standard deviation set by sigma. The edge function in MATLAB determines the gradient by calculating the change in the Gaussian filter. The Canny method has the lowest probability of misrepresenting image noise by employing a two-threshold technique ideal for detecting strong and weak boundaries associated with the mixed properties linked with FYI distribution. (MATLAB Inc. 2019). An example procedure used for OWF area perimeter is shown in Figure 20 and contained in the following syntax: T2 = edge (T2, "canny," T, sigma); where T2 the input SAR image, T is a 1 by 2 vector of the two thresholds (Tlow Thigh) values previously explained, and sigma is the standard deviation of the Gaussian smoothing filter, and T2 is the output image(After applying thresholds to all SAR images, ice feature count calculations for OWF area, OWF area perimeter and ridge length are determined by dividing the number of threshold pixels by the total number of pixels within a specified sector.
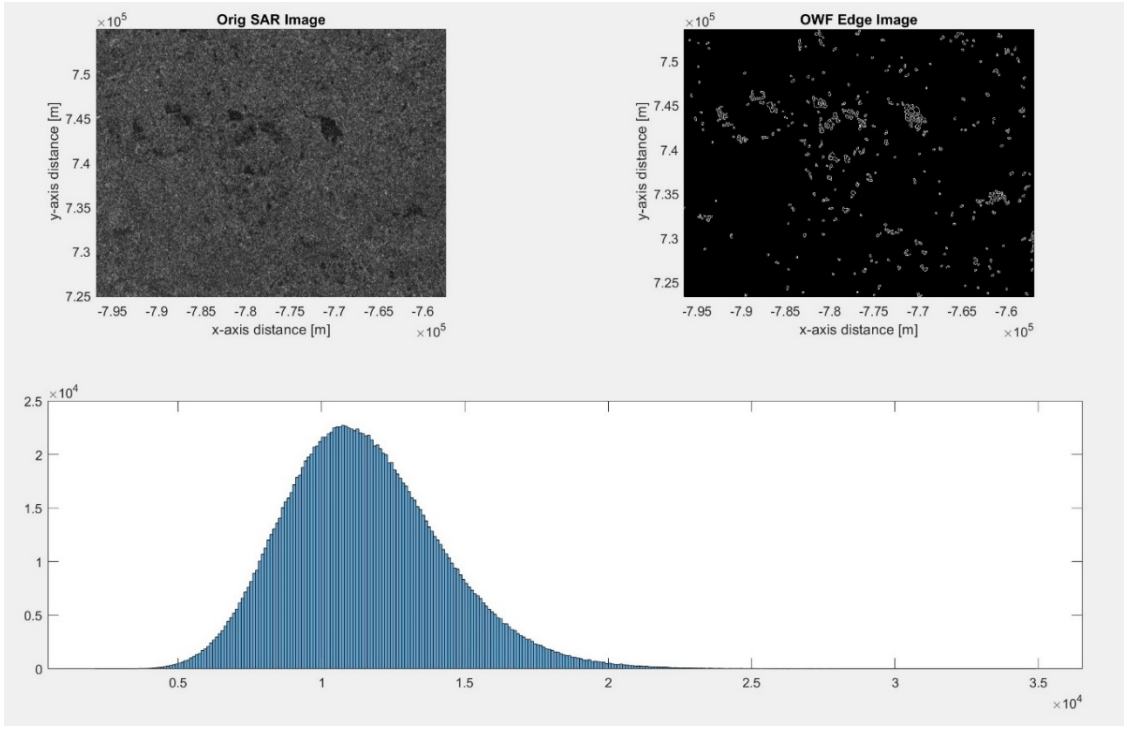
Figure 20.   Schematic outlining OWF area perimeter threshold
determination process.

c.   *Ridge Length Threshold Determination*

High intensity pixels within each SAR images are as ice ridge features. The associated pixel value histogram gain is used to guide a high pixel value threshold for the bright ice ridge features by interactively comparing the original image with the resulting ice ridge mask for different threshold choices (Figure 21).
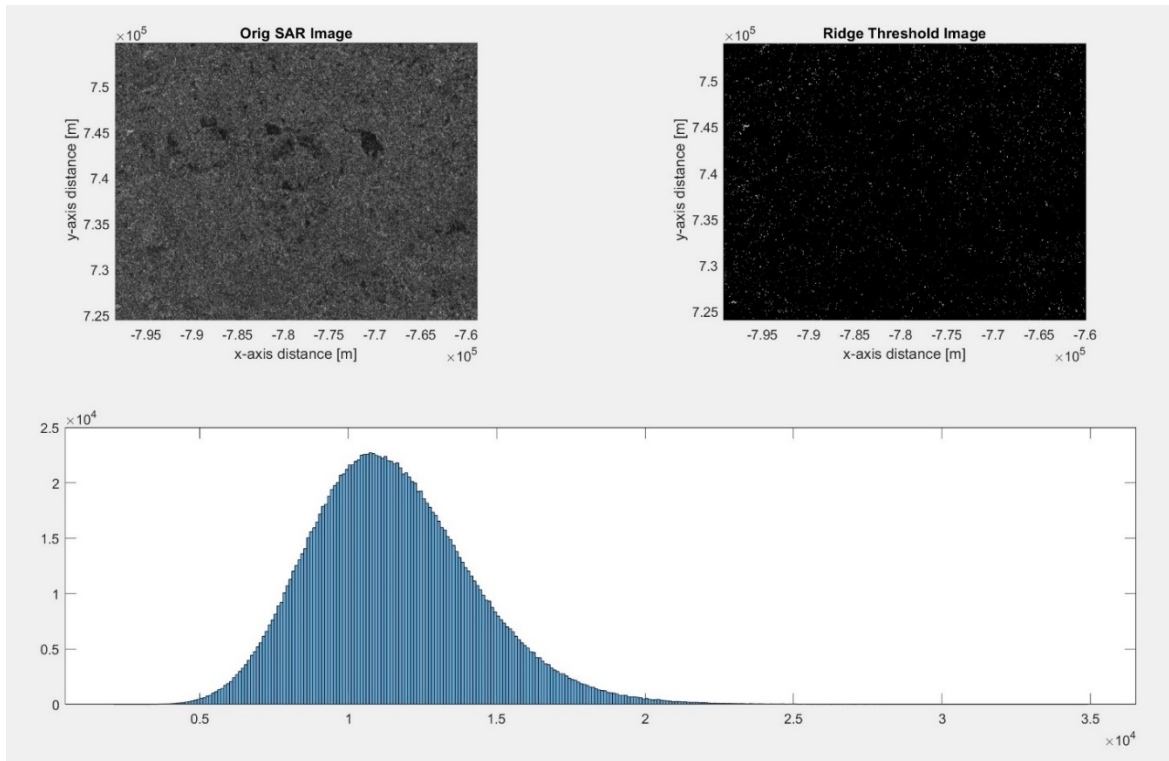
Figure 21.   Schematic outlining ridge length threshold
determination process

The effect of the open water area, open water feature perimeter, and ice ridge concentrations on the measured ocean/ice drag coefficients were explored by measuring these feature concentration in range-binned sectors upstream of the AOFB C_d observations. The available SAR images covering the AOFB / ITP locations during October 2018 in the Beaufort Sea from SODA clusters 2 (AOFB 41) and 3 (AOFB 42) were used in this analysis. Ice current drift bounded by a sector polygon with a 20-degree arc either side forms a series of sector masks that are overlaid on each SAR feature image mask (Figure 22). The pixel counts within the range sector bin are used to normalize feature pixel counts within that sector, resulting in feature concentration estimates at each range bin (Figure 23). The ice in this study area far from coastal boundaries is in free drift, so moves in response to wind forcing events. Surface winds move the ice, and generate a current relative to the ice in nearly the opposite direction, a forming turbulent boundary layer that imposes stress into the ocean below.

39
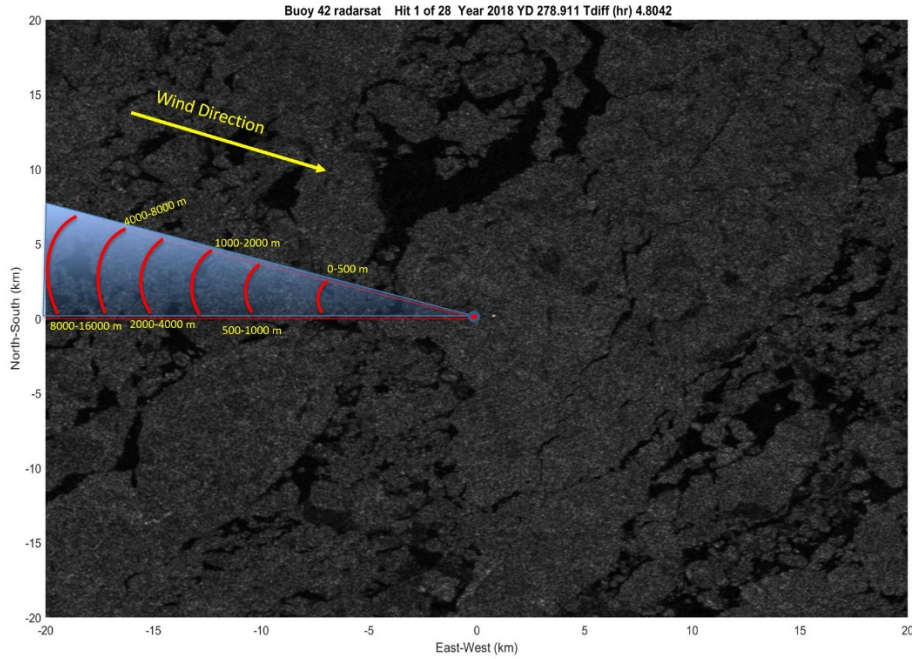
Buoy location at image center (red circle). Upstream analysis field (blue shading). Sector looking angle (two red lines extending from buoy). Wind forcing and current direction (yellow arrows).

Figure 22.   Diagram of the upstream feature analysis.
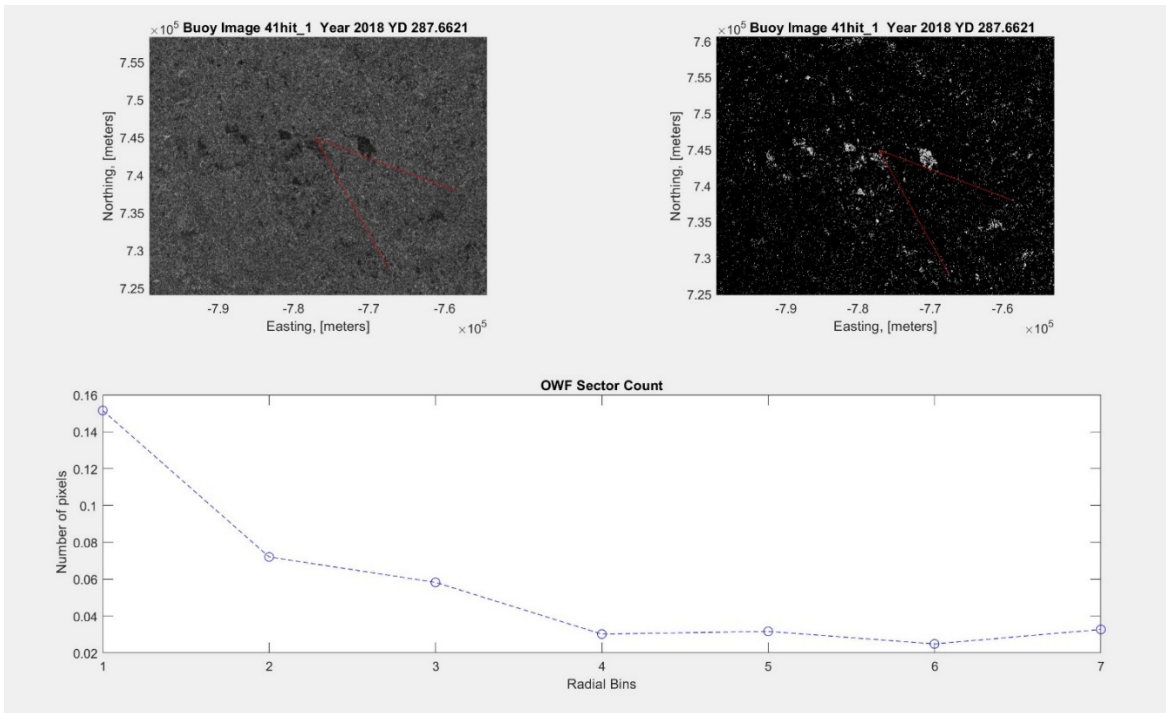
Top left is the original SAR image. Top right is threshold image. Bottom is the OWF area perimeter feature count per radial bin.

Figure 23.   Example of ice feature count plot.

THIS PAGE INTENTIONALLY LEFT BLANK

IV. DATA ANALYSIS AND RESULTS

A. OVERVIEW OF ICE-OCEAN ENVIRONMENTS

1. AOFB 41

SAR images from the start and end of the 15-day long image sequence available for this study (Figure 24) shows the ice pack changes during the October 14, 2018 to October 29, 2018. Dark areas in the image represent open water or new ice. During this time the ice pack distorted significantly in response to moderate wind events. The sea ice landscape is homogeneous at the beginning of the AOFB 41 deployment with SAR imagery indicating ~40-60% FYI and moderate sized OWF. Ice floe distribution consisted of variable sized, 100–300 m ice floes in appearance through the October through early November 2018 study period for AOFB 41. A mixture of circular open water fraction features is in higher concentration at close distances to the AOFB. A nearly uniform distribution of smooth ice, with linear ice ridges seen as very bright lines of pixels is seen throughout the area. The final SAR image (Figure 24 right image) shows a more irregular pattern with a long newly formed ice divergent induced ice leads ~10 km south of the AOFB location. A noticeable change in surface roughness marked by an increase in convergence induced ice ridges ~14 km west of the AOFB location.
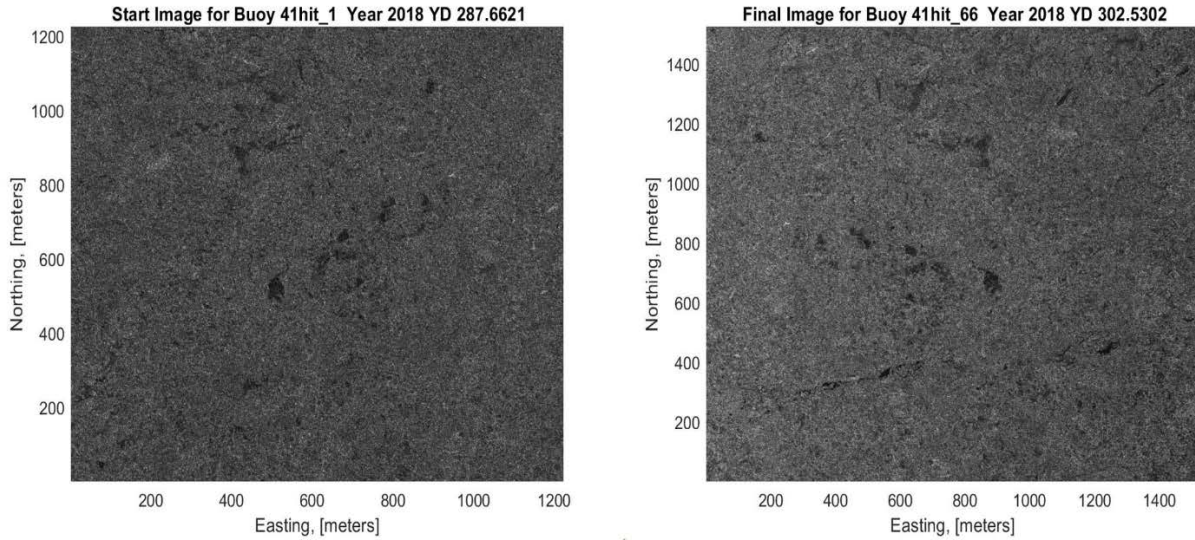
Figure 24. Start (14 October 2018) and final (29 October 2018) SAR images from AOFB 41 deployment

2.   AOFB 42

The AOFB 42 SAR image sequence spanned from October 5, 2018 through October 30, 2018 (Figure 25). The initial SAR image reveals a significantly different sea ice landscape compared with AOFB 41. The ice surface was characterized by medium to large MYI floes in close proximity with smaller fragments with increasing radial distance from the AOFB. Larger and more frequent linear shaped open water areas are seen near the AOFB. These OWF areas become more circular in size and frequency at ~5 km and greater from the AOFB. In contrast to the Buoy 41 deployment, the sea-ice displays a more heterogeneous sea ice field associated with a larger inclusion of MYI floes and smaller fragments. The final SAR image (Figure 25 right image) displays a difference in ice type (more of a FYI appearance) and reduced ice floe distribution consisting of a more homogeneous ice floe appearance. A significant reduction in open water area across the SAR image is likely due to a combination of local ice convergence and the start of ice growth. Ice ridge length increased in size and occurrence in all directions at ~ 14–16 km from the AOFB location. Vivid open water areas seen in the Buoy 42 start image significantly decreased. In contrast to the initial image (Figure 25 left), there are fewer areas of open water near the buoy site (image center) in the final image. SAR imagery for

44

Buoy 42 also reveals an increase in ice ridge length distribution in all directions out from the AOFB again indicating strongly convergent conditions at the end of the study period.
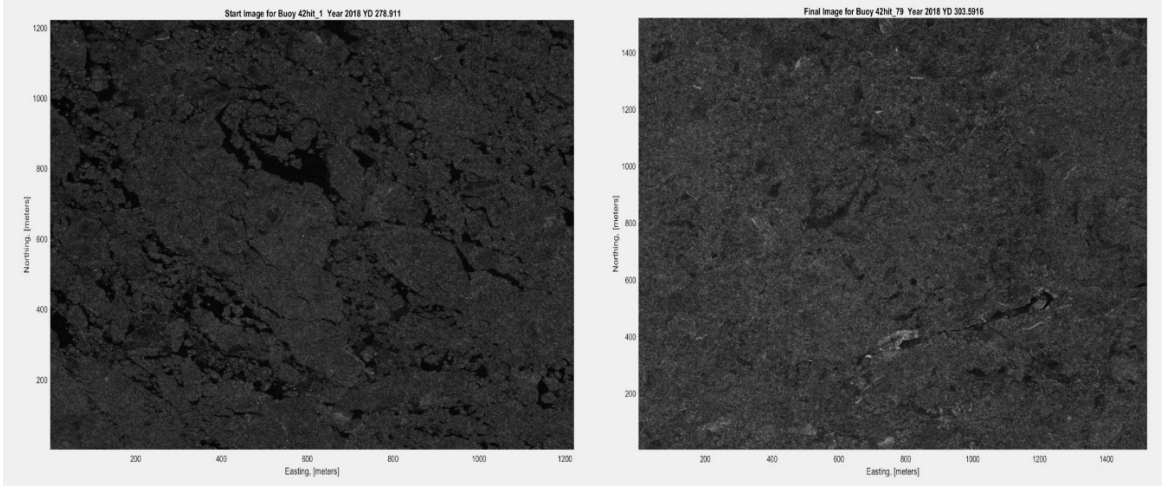

Figure 25.   Start (5 October 2018) and final (30 October 2018)
SAR images from AOFB 42 deployment

THIS PAGE INTENTIONALLY LEFT BLANK

V.   RESULTS AND DISCUSSION

A.   CORRELATION RESULTS

Correlational analyses were used to examine the relationship between calculated ice-ocean drag coefficients and threshold sea ice pixel counts for 6 logarithmic radial bins sector bins centered on the buoy position to explore if there are relationships between observed ocean-ice drag coefficients and upstream measurements of SAR feature densities. A scatter plot for each sector range bin have been calculated with an associated first order linear regression goodness of fit line. Linear correlation coefficient (R) values and error estimates calculated from the MATLAB function *corrcoef* have been calculated for each scatter plot.

1.   Ice-Ocean Drag Coefficients vs. Ice Threshold Feature Counts

Ice-Ocean Drag Coefficient and ice speed are compared across all the available SAR images spanning a 60-day interval for ice speeds greater than 0.05 ms-1 (Figure 26). Drag coefficient values are unreliable to lower mean currents.

The primary hypothesis is that ice-ocean drag coefficients are controlled by SAR-derived ice feature densities in a 40-degree wide sector upstream from the location of the in situ friction velocity measurements. AOFB measurement. Multiple sector range bins are used to test the upstream range of influence for each potential roughness feature. The three features are OWF, open water perimeter fraction, and ridge fraction. Correlation plots (Figures 26, 27, 28, 29) of the relationship between ice-ocean drag coefficient response and ice feature count density at different radial distance test these relationships.
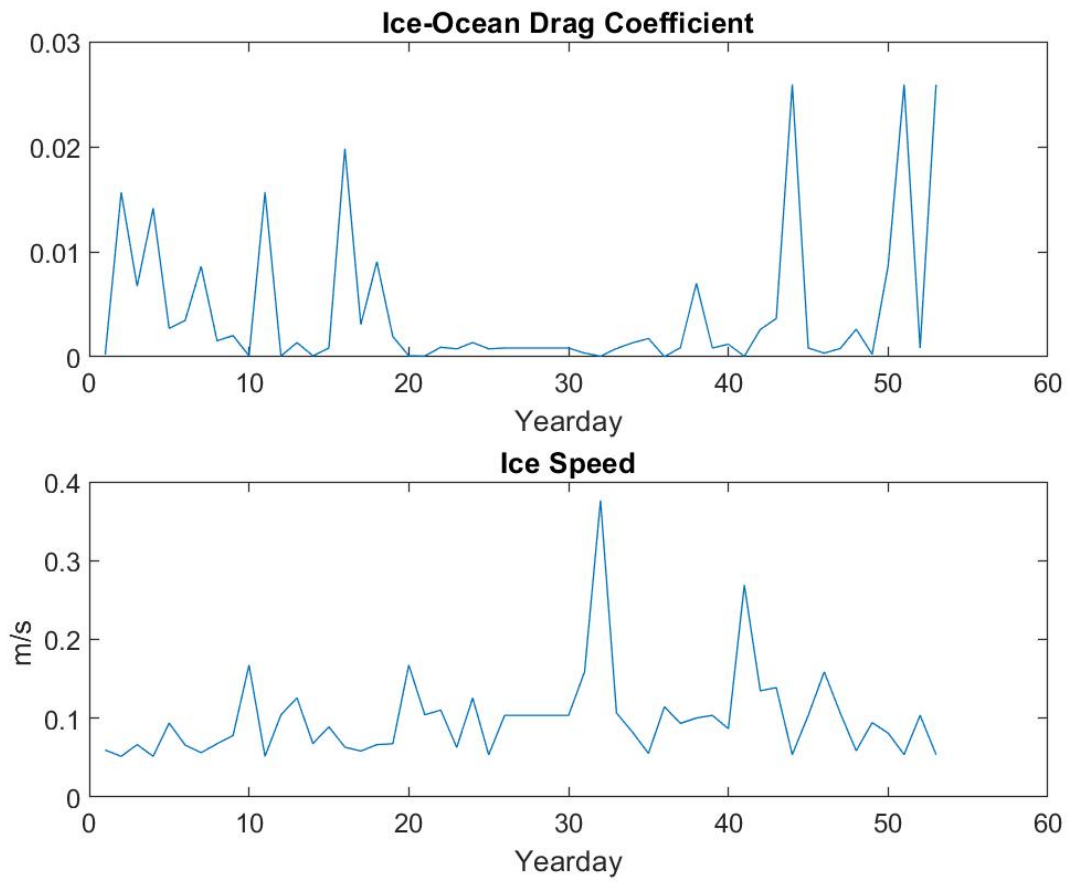
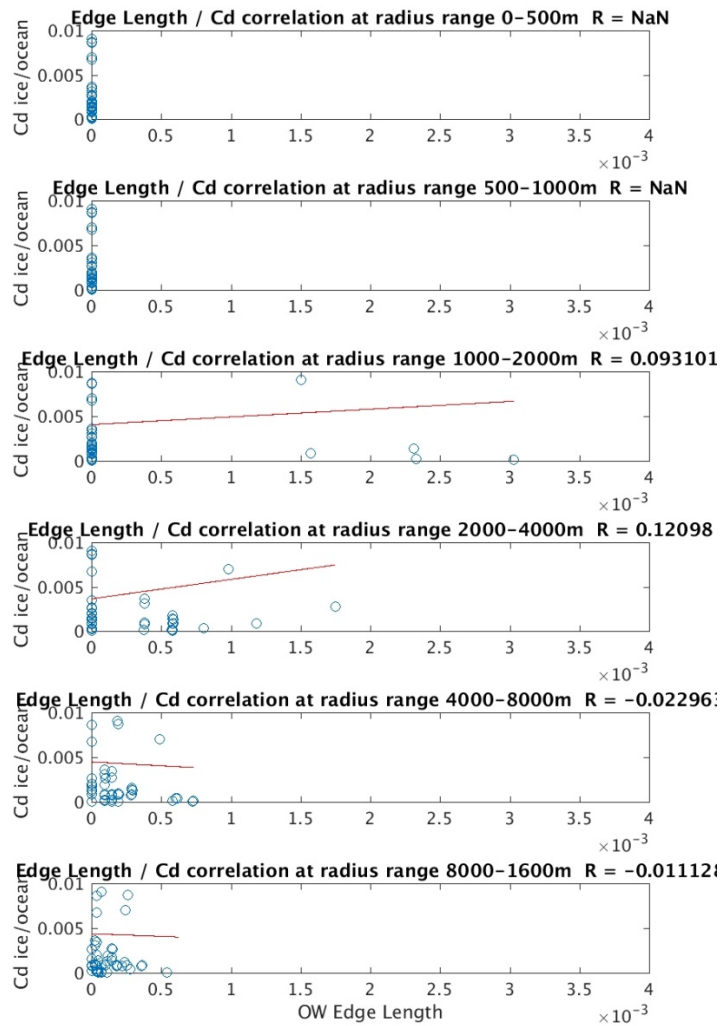Figure 26.   Ice speed vs. ice-ocean drag coefficients

Figure 27.   Ice-ocean coefficient vs. edge length

The comparison between ice-ocean drag coefficients vs. edge length count (Figure 27) has no data entries in the two nearfield range bins covering 0–1000 m. A very weak positive correlation between at 1000–2000 m exist. Overall the data reveals a statistically insignificant relationship between ice-ocean coefficient and edge length count.

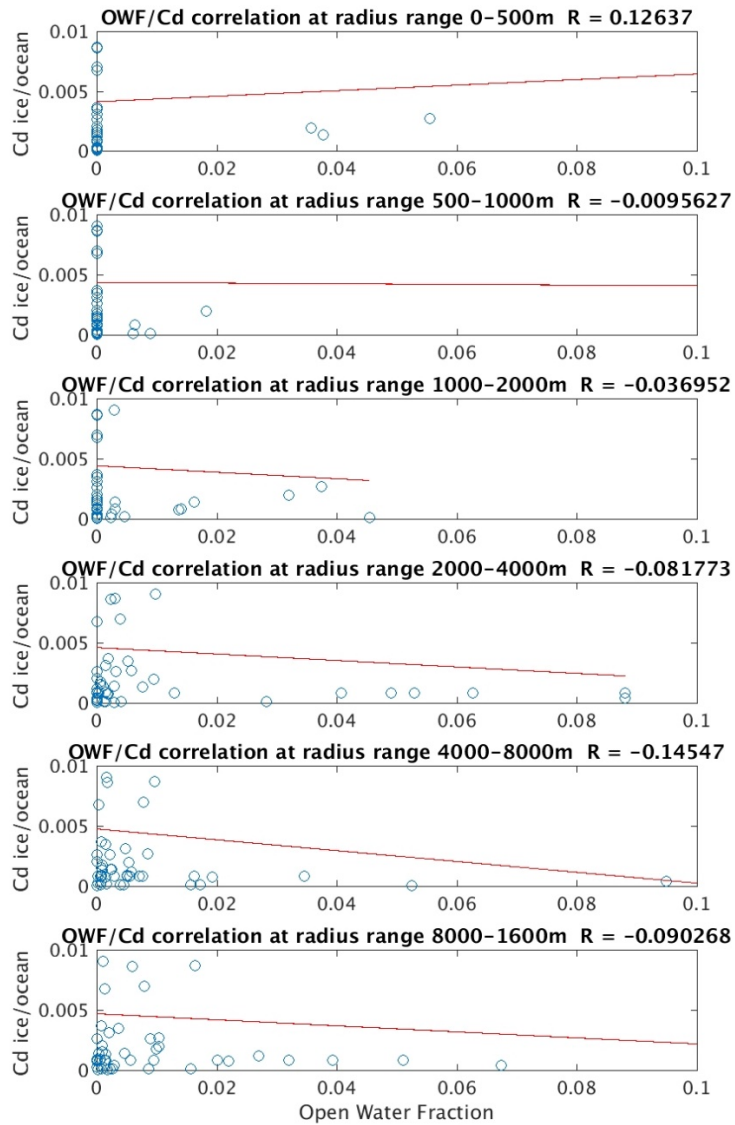Figure 28.   Ice-ocean coefficient vs. OWF area count

The correlation between ice-ocean drag and OWF area count are weakly correlated out to 1000. There is a slight weak negative correlation from 1000 out to 16000 m, but overall the data reveals a statistically insignificant relationship between ice-ocean coefficient and OWF area count due to SAR resolution limitations and near field area. The

large number of zero OWF values reflect either the limited spatial resolution of the OWF estimates or the insensitivity of C_d to the local OWF.
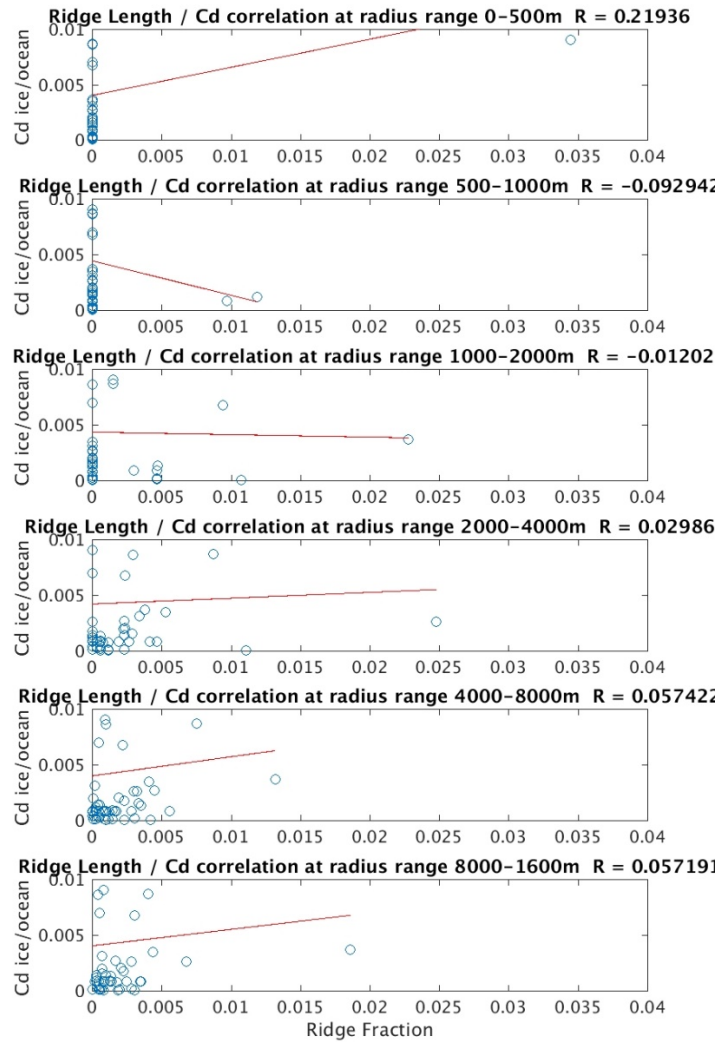

Figure 29.   Ice-ocean coefficient vs. ridge length count

The comparison between ice-ocean drag coefficients vs. ridge length count (Figure 29) shows a weak correlation in the near field from 0–500 m. Correlations become negligible with increasing radial range. Overall the data reveals a statistically insignificant relationship between ice-ocean coefficient and ridge length count.

Figure 30.   Ice-ocean coefficient vs. OWF area count across
total 20x20 km ice field

The comparison between ice-ocean drag coefficients vs. OWF (Figure 30) Correlations are negligible with increasing radial range and overall data reveals a statistically insignificant relationship between ice-ocean coefficient and ridge length count a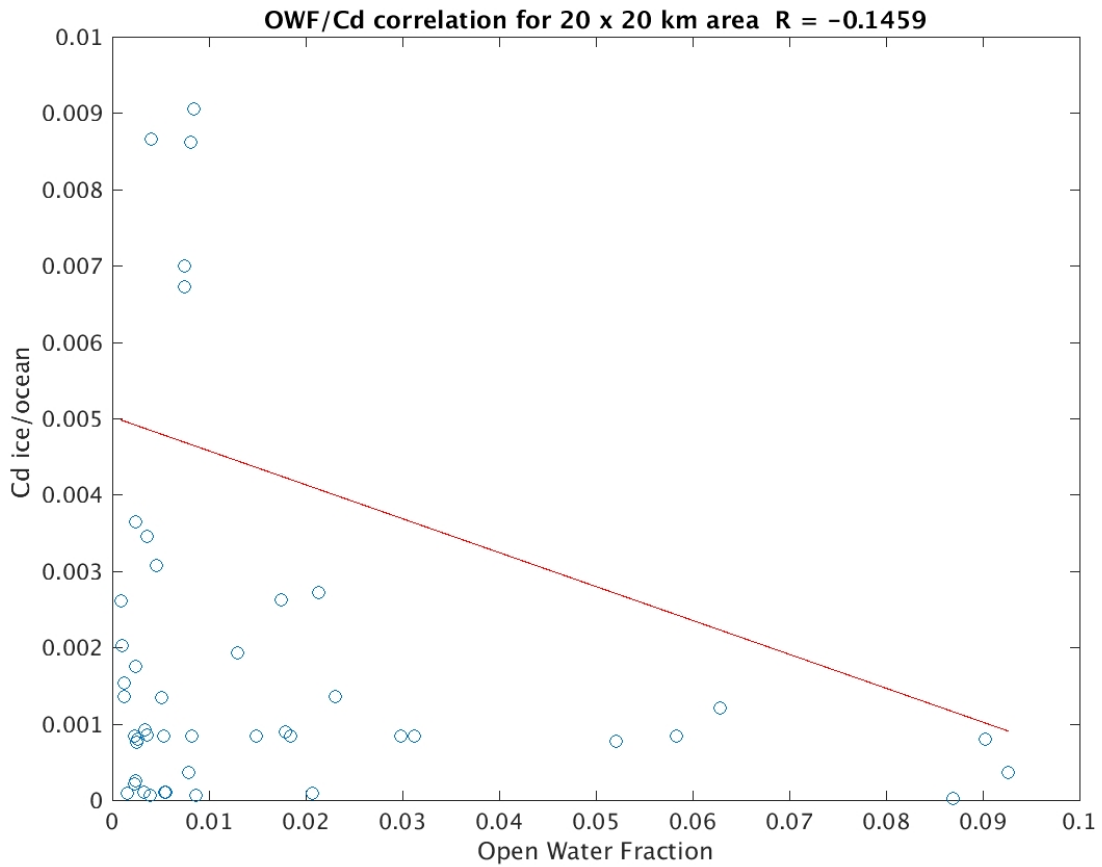cross the total 20x20 km ice field. This is not unexpected as the influence of OWF was expected to be strongest in the near-field just upstream from the AOFB.

Figure 31.　　Ice-ocean drag coefficient vs. edge length count
across total 20x20 km ice field

The comparison between ice-ocean drag coefficients vs. edge length count across the total 20x20 km ice field (Figure 31) shows a lack of predictability between a given ice-ocean drag coefficient for edge density across the large 20 x 20 km domain.
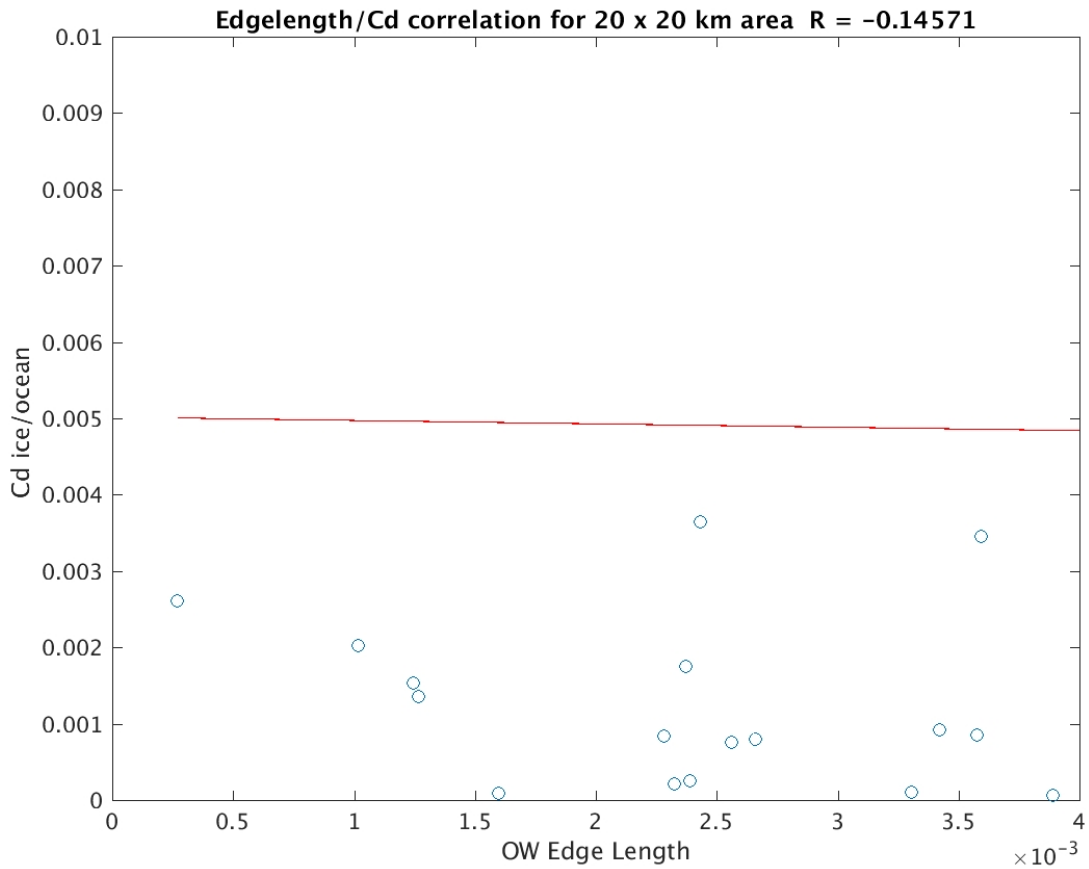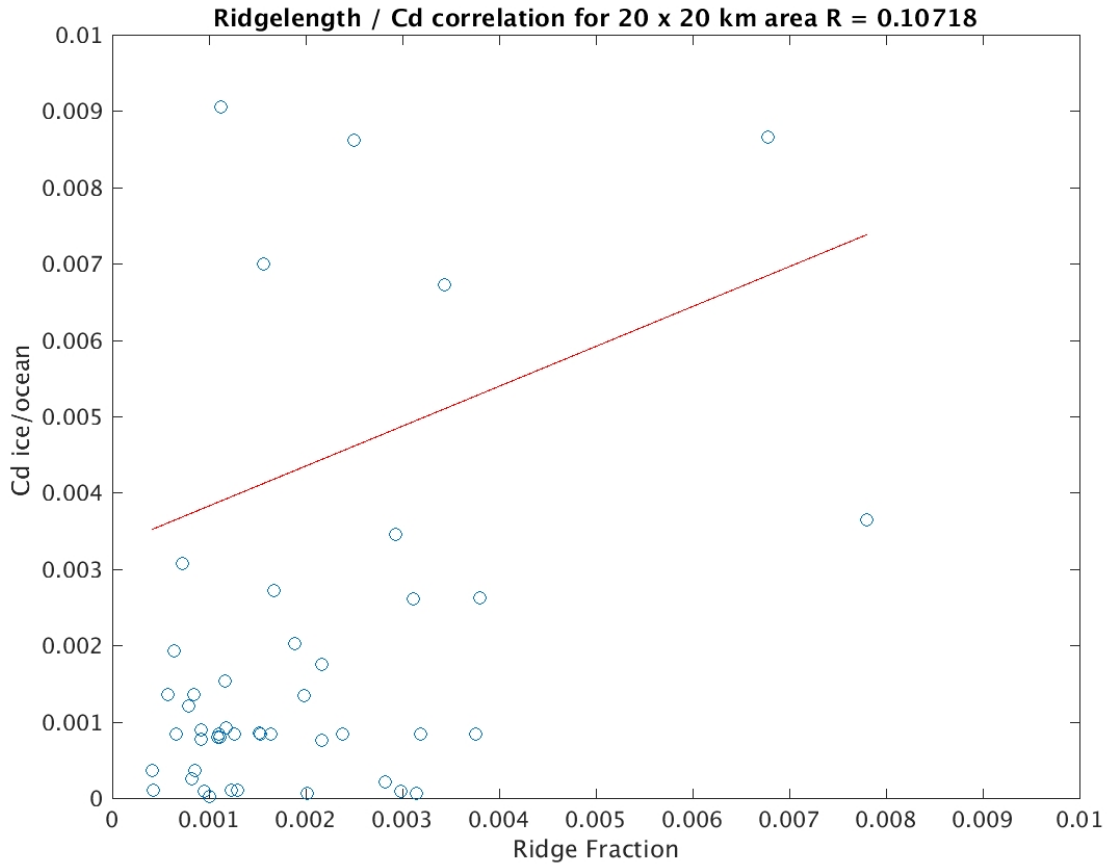
Figure 32.   Ice-ocean drag-coefficient vs. ridge length count
across the total 20x20 ice field

The comparison between ice-ocean drag coefficients vs. ridge length count across the total 20x20 km ice field (Figure 32) shows a weak relationship and statistically insignificant.

VI.   CONCLUSIONS

This study examines relationships between ice-ocean drag coefficients and OWF area, OWF perimeter and ridge length ice feature count using AOFB in-situ measurements collected between 5 October and 29 October 2018 in the Beaufort Sea and Southern Arctic Ocean. Thresholding and image processing techniques were applied to a total of 82 SAR images classify three ice feature types: OWF area, OWF perimeter and ridge length. It was hypothesized that there would be a statistically robust correlation between ice-ocean drag coefficients and the three SAR-derived ice feature densities in an upstream sector centered on the buoy location, with the strongest correlations in the near-field range (0-500 m). However, with the SAR images available to this study, correlations were very weak for all three feature types. Limitations in the analysis technique include the difficulties in determining pixel value thresholds for open water areas and ridges, and a lack of validation of these choices with direct observations of the features. This could be addressed in future studies with visible imagery and ice altimeter data not available here. Additionally, the limited (0–50m square) pixel size of the RADARSAT-2 and Sentinel-1 imagery only marginally resolved features, which is particularly important in the near-filed range which most influence the turbulent boundary layer measured by the AOFB. This was evidenced in all the ice feature count correlation plots, where the near field (0-500 m) radius bins displayed a weak relationship and negligible correlation with increasing distance in all the other bins. Although this is a consistent result, being able to count ice features in the near field, where u_* has a significant footprint influence is the key and justification for high resolution remote sensing systems. The ridge length count vs. coefficient plot result was unexpected in that, there as a stronger relationship between the drag coefficient in the medium ranges (2000–8000 m). Most importantly much longer time series and higher resolution SAR imagery are needed to gather more robust statistical estimates of these correlations.

THIS PAGE INTENTIONALLY LEFT BLANK

VII. FUTURE WORK

An important consideration for future studies would be the employment of higher resolution satellite imagery. All the correlation cases revealed an inability to resolve ice feature counts in the near ice field were friction velocity was most prevalent. This thesis demonstrates that the multi-variate dynamical complexities of the Arctic system. The introduction of machine learning has proven to be a viable source for routine automation such as GPS positioning and feature recognition to identify hidden analysis features and statistics. Another major focus is taking advantage of the vast array of new data being generated from field science expeditions such as Multidisciplinary Drifting Observatory for the Study of Arctic Climate. Four AOFB's have been deployed in the Transpolar Drift as part of the year-long manned ice station, which will have consistent high resolution visible and SAR coverage.

THIS PAGE INTENTIONALLY LEFT BLANK

LIST OF REFERENCES

Aagaarda, K., A. Foldvik, and S. R. Hillman, 1987: The West Spitsbergen Current: Disposition and water mass transformation. *J. Geophys. Res. Ocean.*, **92**, 3778–3784, https://doi.org/10.1029/JC092iC04p03778.

Burnham, J., J. Hardy, K. Meadors, and J. Picone, 1998: A Comparison of the Roberts, Sobel, Robinson, Canny, and Hough image detection algorithms. *Proc. IEEE Southeastcon*, https://doi.org/http://www.isip.piconepress.com/publications/unpublished/conferences/1998/ieee_secon/edge_detection/.

Chief of Naval Operations, *Chief of Naval Operations Navy Strategic Outlook for the Arctic Jan2019.pdf*. https://www.mendeley.com/catalogue/navystrategicoutlookarcticjan2019pdf/.

Cole, S. T., and Coauthors, 2017: Ice and ocean velocity in the Arctic marginal ice zone: Ice roughness and momentum transfer. *Elementa*, **5**, https://doi.org/10.1525/elementa.241.

Curry, J. A., and E. E. Ebert, 1992: Annual cycle of radiation fluxes over the Arctic Ocean: sensitivity to cloud optical properties. *J. Clim.*, **5**, 1267–1280, https://doi.org/10.1175/1520-0442(1992)005<1267:ACORFO>2.0.CO;2.

Defense, S. of, 2017: *National Security Strategy*. 68 pp.

Dierking, W., 2013: Sea ice monitoring by synthetic aperture radar. Oceanography **26**(2):100–111; http://dx.doi.org/10.5670/oceanog.2013.33.

Dorn, W., K. Dethloff, A. Rinke, S. Frickenhaus, R. Gerdes, M. Karcher, and F. Kauker, 2007: Sensitivities and uncertainties in a coupled regional atmosphere-ocean-ice model with respect to the simulation of Arctic sea ice. *J. Geophys. Res. Atmos.*, **112**, 1–16, https://doi.org/10.1029/2006JD007814.

Duliu, O. G., and E. D. Seletchi, 2007: Image processing and data analysis in computed tomography. *Rom. J. Phys.*, **52**, 667–675.

Dyne, M., C. Tsatsoulis, and F. Fetterer, 1998: Analyzing lead information from SAR images. *IEEE Trans. Geosci. Remote Sens.*, **36**, 647660, https://doi.org/10.1109/36.662745.

European Space Agency, 2019: European Space Agency. https://www.esa.int/.

Girard, L., J. Weiss, J. M. Molines, B. Barnier, and S. Bouillon, 2009: Evaluation of high-resolution sea ice models on the basis of statistical and scaling properties of Arctic sea ice drift and deformation. *J. Geophys. Res. Ocean.*, **114**, 1–15, https://doi.org/10.1029/2008JC005182.

Government of Canada, 2019: Government of Canada's Open Government. https://open.canada.ca/en.

Intrieri, J. M., M. D. Shupe, T. Uttal, and B. J. McCarty, 2002: An annual cycle of Arctic cloud characteristics observed by radar and lidar at SHEBA. *J. Geophys. Res. C Ocean.*, **107**, 1–14, https://doi.org/10.1029/2000JC000439.

Kwok, R., 2001: Deformation of the Arctic Ocean Sea Ice Cover between November 1996 and April 1997: A Qualitative Survey. 315–322, https://doi.org/10.1007/978-94-015-9735-7_26.

Kwok, R., E. Rignot, B. Holt, and R. Onstott, 1992: Identification of sea ice types in spaceborne synthetic aperture radar data. *J. Geophys. Res.*, **97**, 2391–2402, https://doi.org/10.1029/91JC02652.

Lee, C. M., and Coauthors, 2016: Stratified Ocean Dynamics of the Arctic : Science and Experiment Plan Applied Physics Laboratory University of Washington.

Lupkes, C., V. M. Gryanik, A. Rösel, G. Birnbaum, and L. Kaleschke, 2013: Effect of sea ice morphology during Arctic summer on atmospheric drag coefficients used in climate models. *Geophys. Res. Lett.*, **40**, 446–451, https://doi.org/10.1002/grl.50081.

Markus, T., and S. T. Dokken, 2002: Evaluation of late summer passive microwave Arctic sea ice retrievals. *IEEE Trans. Geosci. Remote Sens.*, **40**, 348–356, https://doi.org/10.1109/36.992795.

Marques, O., 2011: *Practical image and video processing using MATLAB®*. William T. Rhodes, Ed. John Wiley & Sons, Inc., 3–474 pp.

Martin, T., M. Tsamados, D. Schröder, and D. L. Feltham, 2016: Journal of Geophysical Research: Oceans in Arctic Ocean surface stress: A model study. *J. Geophys. Res. Ocean.*, **121**, 1931–1952, https://doi.org/doi:10.1002/ 2015JC011186.

Maslowski, Wieslaw, Marble, Douglas, Walczowski, Waldemar, Schauer, Ursula, Clement, Jaclyn, and Semtner, A., 2004: On climatological mass, heat, and salt transports through the Barents Sea and Fram Strait from a pan-Arctic coupled ice-ocean model simulation. *J. Geophys. Res.*, **109**, 16, https://doi.org/10.1029/2001JC001039.

Maslowski, W., 2014: *The pacific arctic region: Ecosystem status and trends in a rapidly changing environment*. 1–450 pp., J. Clement Kinney, M. Higgins, and A. Roberts, 2012: The Future of Arctic Sea Ice. *Annu. Rev. Earth Planet. Sci.*, **40**, 625–654, https://doi.org/10.1146/annurev-earth-042711-105345.

Matrix Laboratory 2019: Matrix Laboratory (MATLAB). https://www.mathworks.com/products/matlab.html.

Mcphee, M. G., 2008: *Air-Ice-Ocean Interaction: Turbulent Ocean Boundary Layer Exchange Processes*. 215 pp.

McPhee, M. G., T. P. Stanton, J. H. Morison, and D. G. Martinson, 1998: Freshening of the upper ocean in the Arctic: Is perennial sea ice disappearing? *Geophys. Res. Lett.*, **25**, 1729–1732, https://doi.org/10.1029/98GL00933.

Meyer, 2019: Spaceborne Synthetic Aperture Radar: Principles, Data Access, and Basic Processing Techniques. *The SAR Handbook: Comprehensive Methodologies for Forest Monitoring and Biomass Estimation*, p. 44.

Morison, J., K. Aagaard, and M. Steele, 1999: Recent environmental changes in the Arctic: A review. *Arctic*, **53**, 359–371.

National Snow and Ice Data Center, 2019: National Snow and Ice Data Center. https://nsidc.org.

RFE/RL, 2019: Radio Free Europe/Radio Liberty. https://www.rferl.org/a/russia-launches-new-icebreaker-as-it-seeks-to-dominate-arctic-as-ice-retreats/29963437.html.

Rinke, A., W. Maslowski, K. Dethloff, and J. Clement, 2006: Influence of sea ice on the atmosphere: A study with an Arctic atmospheric regional climate model. *J. Geophys. Res. Atmos.*, **111**, 1–14, https://doi.org/10.1029/2005JD006957.

Schuepp, P. H., M. Y. Leclerc, J. I. MacPherson, and R. L. Desjardins, 1990: Footprint prediction of scalar fluxes from analytical solutions of the diffusion equation. *Boundary-Layer Meteorol.*, **50**, 355–373, https://doi.org/10.1007/BF00120530.

Serreze, M. C., and R. G. Barry, 2011: Processes and impacts of Arctic amplification: A research synthesis. *Glob. Planet. Change*, **77**, 85–96, https://doi.org/10.1016/j.gloplacha.2011.03.004.

Shaw, W. J., T. P. Stanton, M. G. McPhee, and T. Kikuchi, 2008: Estimates of surface roughness length in heterogeneous under-ice boundary layers. *J. Geophys. Res. Ocean.*, **113**, 1–16, https://doi.org/10.1029/2007JC004550., J. H. Morison, and D. G. Martinson, 2009: Role of the upper ocean in the energy budget of Arctic sea ice during SHEBA. *J. Geophys. Res. Ocean.*, **114**, 1–21, https://doi.org/10.1029/2008JC004991.

Shawn G. Gallaher, Timothy P. Stanton, William J. Shaw, Sylvia T. Cole, John M. Toole, Jeremy P. Wilkinson, Ted Maksym, and B. H., 2016: Evolution of a Canada Basin ice-ocean boundary layer and mixed layer across a developing thermodynamically forced marginal ice zone. *J. Geophys. Res. Ocean.*, **121**, 4097–4127, https://doi.org/10.1002/2016JC011778.Received.

Stanton, Timothy P., Shaw, B., Naval Postgraduate School Autonomous Ocean Flux Buoy. https://www.oc.nps.edu/~stanton/fluxbuoy/index.html.

Taylor, P. C., M. Cai, A. Hu, J. Meehl, W. Washington, and G. J. Zhang, 2013: A decomposition of feedback contributions to polar warming amplification. *J. Clim.*, **26**, 7023–7043, https://doi.org/10.1175/JCLI-D-12-00696.1.

Tschudi, M. A., J. A. Curry, and J. A. Maslanik, 1997: Determination of areal surface-feature coverage in the Beaufort Sea using aircraft video data. *Ann. Glaciol.*, **25**, 434–438, https://doi.org/10.3189/s0260305500014415.

Wadhams, P., 2003: https://www.pmel.noaa.gov/arctic-zone/essay_wadhams.html.

Walsh, J. E., and W. L. Chapman, 1998: Arctic cloud-radiation-temperature associations in observational data and atmospheric reanalyses. *J. Clim.*, **11**, 3030–3045, https://doi.org/10.1175/1520-0442(1998)011<3030:ACRTAI>2.0.CO;2.

Woods Hole Oceanographic Institution (WHOI), Ice-Tethered Profiler. https://www.whoi.edu/page.do?pid=20756.

Zhang, Qin and Skjetne, R., 2018: *Sea Ice Image Processing with MATLAB*. Taylor and Francis Group, LLC, 1–242 pp.

INITIAL DISTRIBUTION LIST

1.   Defense Technical Information Center
        Ft. Belvoir, Virginia

2.   Dudley Knox Library
        Naval Postgraduate School
        Monterey, California